Birth of an ocean in the Red Sea: Initial pangs

Marco Ligi
Istituto di Scienze Marine, CNR, Via Gobetti 101, IT–40129 Bologna, Italy
(marco.ligi@bo.ismar.cnr.it)

Enrico Bonatti
Istituto di Scienze Marine, CNR, Via Gobetti 101, IT–40129 Bologna, Italy

Lamont Doherty Earth Observatory, Earth Institute at Columbia University, Palisades, New York 10964, USA

Giovanni Bortoluzzi
Istituto di Scienze Marine, CNR, Via Gobetti 101, IT–40129 Bologna, Italy

Anna Cipriani
Lamont Doherty Earth Observatory, Earth Institute at Columbia University, Palisades, New York 10964, USA

Dipartimento di Scienze Chimiche e Geologiche, Università di Modena e Reggio Emilia, L.go S. Eufemia 19, IT–41100 Modena, Italy

Luca Cocchi
Istituto Nazionale di Geofisica e Vulcanologia, Roma2, Via Pezzino Basso 2, IT-19020 Fezzano, Italy

Fabio Caratori Tontini
Ocean Exploration Section, GNS Science, 1 Fairway Drive, Avalon, Lower Hutt 5040, New Zealand

Eugenio Carminati
Dipartimento di Scienze della Terra, Università di Roma "La Sapienza," P.le A. Moro 5, IT-00185 Roma, Italy

Luisa Ottolini
Istituto di Geoscienze e Georisorse, CNR, Via Ferrata 1, IT-27100 Pavia, Italy

Antonio Schettino
Dipartimento di Scienze della Terra, Università di Camerino, Via Gentile III da Varano, IT-62032 Camerino, Italy

[1] We obtained areal variations of crustal thickness, magnetic intensity, and degree of melting of the sub-axial upwelling mantle at Thetis and Nereus Deeps, the two northernmost axial segments of initial oceanic crustal accretion in the Red Sea, where Arabia is separating from Africa. The initial emplacement of oceanic crust occurred at South Thetis and Central Nereus roughly $\sim$2.2 and $\sim$2 Ma, respectively, and is taking place today in the northern Thetis and southern Nereus tips. Basaltic glasses major and trace element composition suggests a rift-to-drift transition marked by magmatic activity with typical MORB signature, with no contamination by continental lithosphere, but with slight differences in mantle source composition and/

or potential temperature between Thetis and Nereus. Eruption rate, spreading rate, magnetic intensity, crustal thickness and degree of mantle melting were highest at both Thetis and Nereus in the very initial phases of oceanic crust accretion, immediately after continental breakup, probably due to fast mantle upwelling enhanced by an initially strong horizontal thermal gradient. This is consistent with a rift model where the lower continental lithosphere has been replaced by upwelling asthenosphere before continental rupturing, implying depth-dependent extension due to decoupling between the upper and lower lithosphere with mantle-lithosphere-necking breakup before crustal-necking breakup. Independent along-axis centers of upwelling form at the rifting stage just before oceanic crust accretion, with buoyancy-driven convection within a hot, low viscosity asthenosphere. Each initial axial cell taps a different asthenospheric source and serves as nucleus for axial propagation of oceanic accretion, resulting in linear segments of spreading.

1. Introduction

[2] Mechanisms of steady state crustal accretion at mid-ocean ridges are rather well established; less is known on the initial processes of oceanic crust production, the transition from rifting to spreading and the relationship between rifting and magmatism. Rifts range from narrow and "magma-rich" (volcanic margins) with high melt production, to wide and "magma-starved" (non-volcanic margins) with almost no rift or post-rift volcanism and sometime a zone of exhumed continental mantle [*Boillot et al.*, 1980, 1987; *Eldholm and Grue*, 1994; *Hopper and Buck*, 1998; *Whitmarsh et al.*, 2001; *Reston and Morgan*, 2004; *Lavier and Manatschal*, 2006; *Huismans and Beaumont*, 2011]. Rate and depth distribution of magma emplacement at rift axis may influence the style of faulting during rifting [*Bialas et al.*, 2010]. Based on observations from North Atlantic and Indian Ocean's margins, mantle temperature and rift history have been suggested as primary factors controlling initial magmatic production [*Pedersen and Skogseid*, 1989; *White and McKenzie*, 1989; *Nielsen and Hopper*, 2004; *Armitage et al.*, 2009, *Armitage et al.*, 2010], whereas from observations in the Gulf of California and Iberia-Newfoundland margins, mantle source composition (depletion vs fertility) has been proposed as a major factor [*Lizarralde et al.*, 2007; *Müntener and Manatschal*, 2006].

[3] Nowhere in today's Earth can the transition from continental to oceanic rift be studied better than in the Red Sea, where Arabia is separating from Africa. Fieldwork in the Red Sea region has fallen almost to a standstill in the recent past due to the political situation in the region. However, we managed in 2005 to run with the *R/V Urania* a geophysical expedition to the axial zone of the central/northern Red Sea, where the initial breakthrough of oceanic crust is occurring today (Figure 1). This paper, based mostly on data obtained during this fieldwork, contributes to our understanding of the earliest stages in the accretion of oceanic lithosphere in the Red Sea, using a combined geophysical/geochemical approach.

1.1. Red Sea

[4] East Africa hosts a network of rifts in different stages of evolution, from fully continental (East African Rift) to fully oceanic (Gulf of Aden), with Afar and the Red Sea in intermediate stages of transition from continental to oceanic. This rift system has been fragmenting the Nubian and Arabian shields since late Oligocene-Miocene [*Kroner et al.*, 1987; *Sultan et al.*, 1993; *Ghebreab*, 1998; *Stern*, 1994].
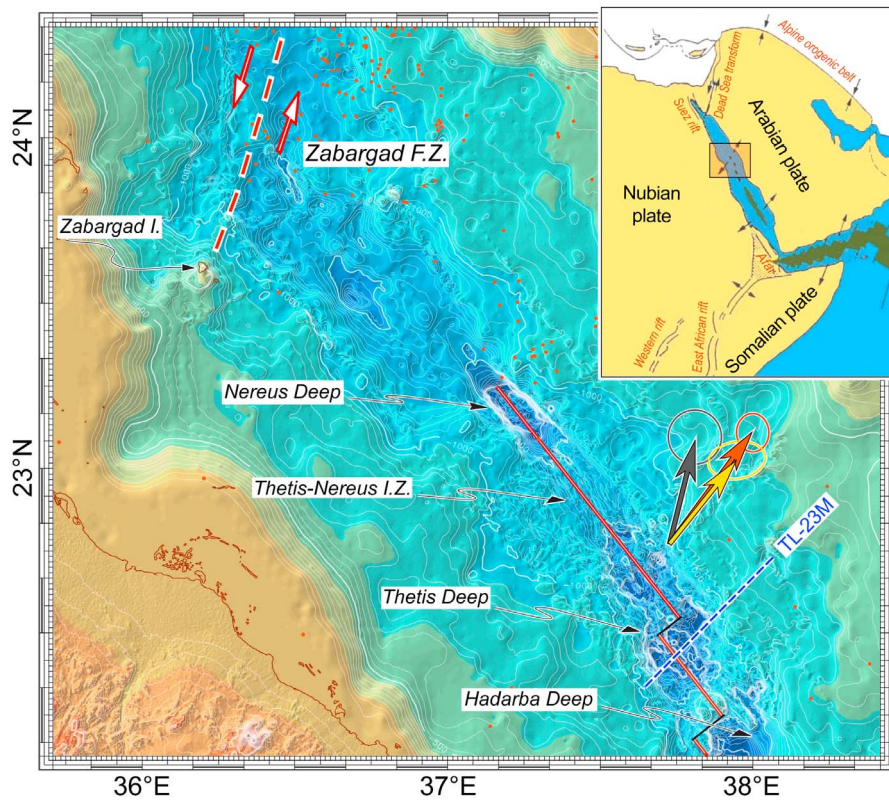
Figure 1. Topography of the northern-central Red Sea. Red dots, earthquake epicenters from the International Seismological Data Centre. Thick red dashed line: Zabargad fracture zone. Red solid lines: axes of Nereus and Thetis segments. Location of seismic reflection profile TL-23 M (see Figure 3) is indicated. Dark gray, orange and yellow arrows indicate velocity vectors of Arabia relative to the Nubia plate from NUVEL1 [*DeMets et al.*, 1994], *McClusky et al.* [2003], and *Chu and Gordon* [1998], with full spreading rates of 9.7, 9.4 and 12.2 mm/a, respectively. Top right inset: simplified plate tectonic framework of the Red Sea/Gulf of Aden area: dark green areas, oceanic crust.

[5] The separation of Arabia from Nubia involved a counter-clock rotation of Arabia relative to Nubia, resulting in decreasing spreading rates and total extension from south to north, which continues to the present. Fission track data suggest two distinct phases of uplift and erosion of rift shoulders during the early stages of Red Sea rifting [*Omar and Steckler*, 1995]. The first phase began ~34 Ma, although there is no dated sedimentary evidence of significant uplift and erosion at this time [*Bosworth et al.*, 2005]. The second phase, in early Miocene (25 to 21 Ma), marked the beginning of the main stage of extension [*Omar and Steckler*, 1995], with syn-rift sediments distributed along the entire length of the Red Sea [*Bosworth et al.*, 2005]. Extension in the Gulf of Suez, initially the northern end of the Red Sea, decreased rapidly in Middle Miocene [*Moretti and Colletta*, 1987; *Steckler et al.*, 1988] due to a sinistral strike-slip displacement along the Gulf of Aqaba-Dead Sea, a new

transform boundary linking the Red Sea to the convergent Bitlis-Zagros plate boundary [*Freund et al.*, 1968; *Khalil and McClay*, 2001].

[6] The Red Sea basin is characterized by: (a) shallow continental shelves; (b) a ~200 km wide, 600–1000 m deep main depression, with smooth topography, extending over the entire length of the basin (~2000 km); and (c) a narrow axial valley (continuous from 15°N to 18°N, intermittent up to 24°N, absent north of 24°N). The axial valley, about 2000 m deep and <50 km wide, is carpeted by oceanic basalt and flanked by Vine-Matthews magnetic anomalies [*Drake and Girdler*, 1964; *Coleman*, 1974; *Roeser*, 1975]. Morphology reflects along strike variations in rifting stages, with the southern Red Sea having already a well developed oceanic rift since up to 5 Ma. Seafloor spreading becomes discontinuous in the central Red Sea where the emplacement of oceanic crust starts in

discrete axial cells [*Bonatti*, 1985], and is absent in the northern Red Sea (Figure 1), although scattered basaltic intrusions have been observed there [*Cochran*, 2005].

[7] The Red Sea region is underlain by Miocene and younger sediments [*Sestini*, 1965; *Whiteman*, 1968], with evaporites reaching a thickness of up to 7 km [*Sestini*, 1965; *Said*, 1969; *Girdler and Styles*, 1974; *Searle and Ross*, 1975], followed by Pliocene pelagic carbonate oozes. The unconformity at the base of post-evaporitic sediments, verified during DSDP Leg 23 [*Whitmarsh et al.*, 1974], is well documented in seismic profiles and has been designated as reflector "S." Salt diapirism is also shown on seismic reflection profiles [*Izzeldin*, 1982; *Ross and Schlee*, 1973].

1.2. Volcanism and Afar Mantle Plume

[8] The impingement from below of the Afar mantle plume, starting roughly 31 Ma [*Hofmann et al.*, 1997; *Storey*, 1995; *Ebinger and Sleep*, 1998], may have influenced the evolution of the Red Sea rift system. The onset of rifting in the Red Sea was preceded by flood basalts erupted in Ethiopia, NE Sudan and SW Yemen, followed by rhyolitic volcanism until ~26 Ma [*Baker et al.*, 1996]. Little significant volcanic activity occurred within the central and northern Red Sea during the rifting stage, except for 24–21 Ma dike intrusions along the Arabian margin [*Bartov et al.*, 1980; *Feraud et al.*, 1991]. This diking episode, suggestive of a dramatic increase in the extension rate [*Pallister et al.*, 1987], was accompanied in the southern Red Sea by local intrusion of granitic to gabbroic plutons [*Pallister*, 1987]. Basaltic volcanism continued from Late Oligocene to the present in Afar and Southern Yemen [*Zumbo et al.*, 1995; *Coulie et al.*, 2003], as well as in the Arabian plate, outside the Red Sea rift, with flood basalt provinces known as Harrats [*Coleman and McGuire*, 1988; *Pallister et al.*, 2010]. A dike intruded in the Harrat Lunayyir lava field as recently as 2009 [*Pallister et al.*, 2010]. Active extension by means of dike intrusions in the Arabian plate about 200 km from the Red Sea axis has been tied, based on seismic tomography, to a N-S thermal mantle anomaly flowing away from the Afar hot spot not below the Red Sea, but beneath the Arabian plate [*Hansen et al.*, 2007; *Chang and Van der Lee*, 2011]. The location of this channel is marked by volcanic rocks erupted since Late Oligocene, with older flows trending parallel to the Red Sea (NNW-SSE) but younger flows oriented more northerly (N-S),

suggesting that the mantle thermal anomaly moves with Arabia [*Chang et al.*, 2011].

2. Methods and Data

[9] We carried out in 2005 with the *R/V Urania* (cruise RS05) multibeam, magnetic and multichannel seismic reflection surveys as well as bottom rock sampling, focusing on the two northernmost Red Sea axial oceanic segments, i.e., Thetis and Nereus Deeps (Figure 1).

2.1. Bathymetry

[10] Bathymetry was acquired with a RESON SeaBat 8160 multibeam, DGPS positioning, and TSS MAHRS MRU and gyrocompass (Figure 2a). Data, processed by the Kongsberg Neptune package, produced Digital Terrain Models of Thetis and Nereus Deeps with up to 25 m of grid resolution. Topography of the northern central Red Sea (Figure 1) was obtained from a synthesis of our own multibeam and single-beam data [*Bonatti et al.*, 1984] acquired in 1979 (*R/V Salernum*, MR79) and 1983 (*R/V Bannock*, MR83), plus data of *Pautot* [1983], GEBCO (https://www.bodc.ac.uk/data/) and NGDC (http://www.ngdc.noaa.gov/mgg/) databases; and elevation data from the Shuttle Radar Topography Mission (SRTM) database (http://srtm.usgs.gov/). Spatial analysis and mapping were performed using the PLOTMAP package [*Ligi and Bortoluzzi*, 1989].

2.2. Seismic Reflection and Sediment Thickness

[11] Our multichannel seismic reflection survey employed a Teledyne 48-channel streamer (12.5 m group interval) and a 2 Sercel GI-GUN tuned array (air capacity: 7 l, pressure: 2000 psi). Shot interval was set at 50 m, and seismic data were digitized and stored by a Geometrics Stratavisor at 1 ms sampling rate. Three lines (6 total) were run across Thetis Deep. Single channel 30 kJ sparker data were shot during MR79 and MR83 cruises on the Thetis-Nereus inter-trough zone, Nereus Deep and in the area between Nereus and the Zabargad fracture zone [*Bonatti et al.*, 1984]. Multichannel seismic data have been processed using an industrial package (Disco/Focus) by Paradigm Geophysical, following a standard sequence up to time migration. Processing of the data includes: trace editing, spherical divergence gain recovery, gapped deconvolution, common mid-point gather sorting, velocity
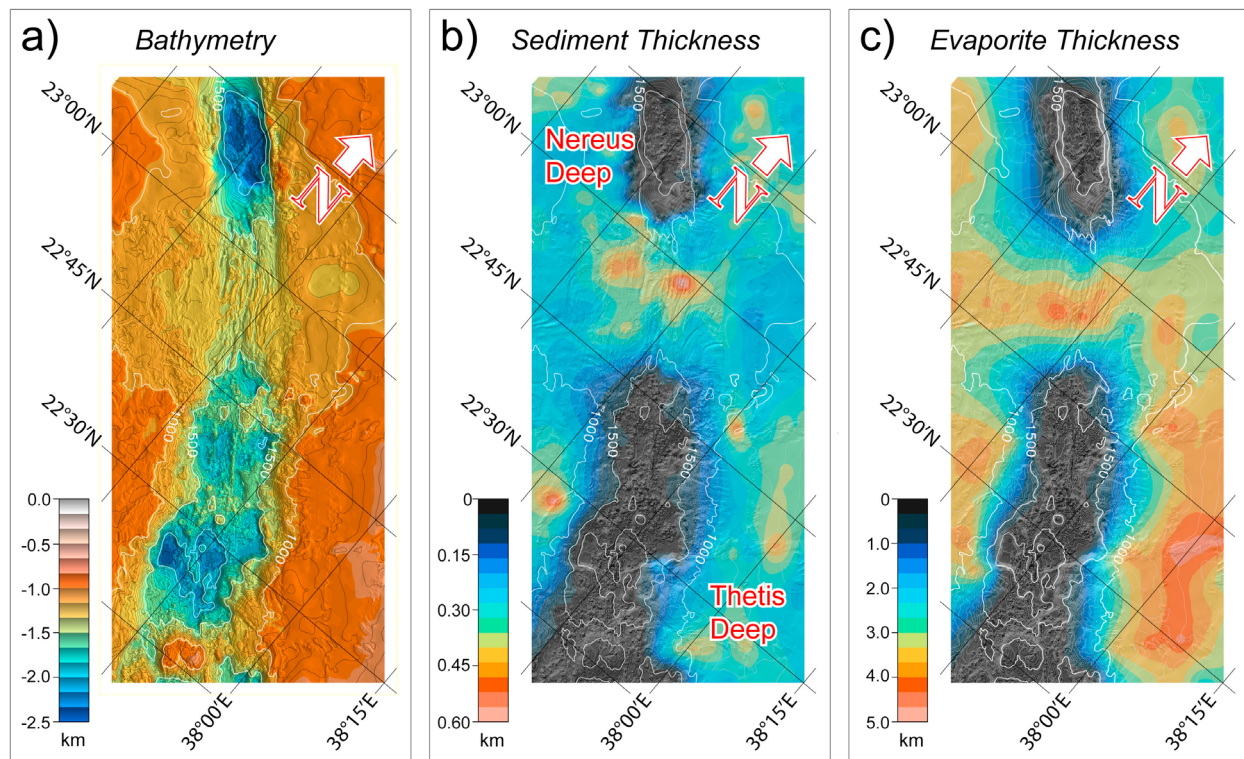
Figure 2. (a) Shaded relief image from swath bathymetry (source of light from NE) showing that the Thetis segment consists of three right-stepped sub-basins. Grid resolution 25 m. Color bar in km below sea level. (b) Plio-Quaternary hemipelagic cover thickness. We assumed reflector "S" as the base of post-evaporite sediments. (c) Thickness of Miocene sediments including salt and layered evaporites. Plio-Quaternary and Miocene isopachs are superimposed on bathymetry.

analysis, dip and normal move out corrections, multiple suppression by predictive deconvolution in tau-p domain, stacking, time variant filtering, and finite difference time migration.

[12] Thickness of hemipelagic cover and evaporitic layers has been estimated from refraction data of *Tramontini and Davis* [1969], our own multichannel (RS05) and single-channel seismic (MR79, MR83) reflection data and those of *Izzeldin* [1982, 1987, 1989], adopting average interval seismic velocities of 2 km/s and 3.75 km/s, respectively [*Tramontini and Davis*, 1969]. The post-evaporitic sequence has a nearly uniform thickness of about 0.2 km, except in the center of the Nereus-Thetis intertrough zone where the thickness increases up to 0.6 km and near the axial trough where it thins down to <0.1 km. On both sides of the axial trough it is thinner than average and remarkably disturbed (Figure 2b). The Miocene evaporites below reflector "S" show two different seismic facies. One is represented by regions rich of reflectors corresponding to layered evaporites (from borehole data they are made up of anhydrite, salt, mudstone and sandstone) with

an average seismic velocity ranging between 3.0 and 3.5 km/s. The other includes regions almost devoid of reflectors corresponding to rock salt with an average velocity of 4.2–4.6 km/s (Figure 3). The layered evaporites are always surrounded and underlain by rock salt with salt increasing toward the axial trough [*Izzeldin*, 1982, 1987]. The thickness of the Miocene section is maximum below the flanks of the main depression and in the center of the Thetis-Nereus inter-trough zone, where it can reach more than 5 km; it thins approaching the axial troughs (Figure 2c).

2.3. Magnetics

[13] Cruise RS05 total-field magnetic data were corrected for diurnal variations using reference data from the Addis Abeba and Qsaybeh observatories. Magnetic anomalies were obtained removing the international geomagnetic reference field (IGRF) and were gridded at 1 km step together with data from cruise MR83 and NGDC database, in order to obtain better lateral coverage (Figure 4a). The
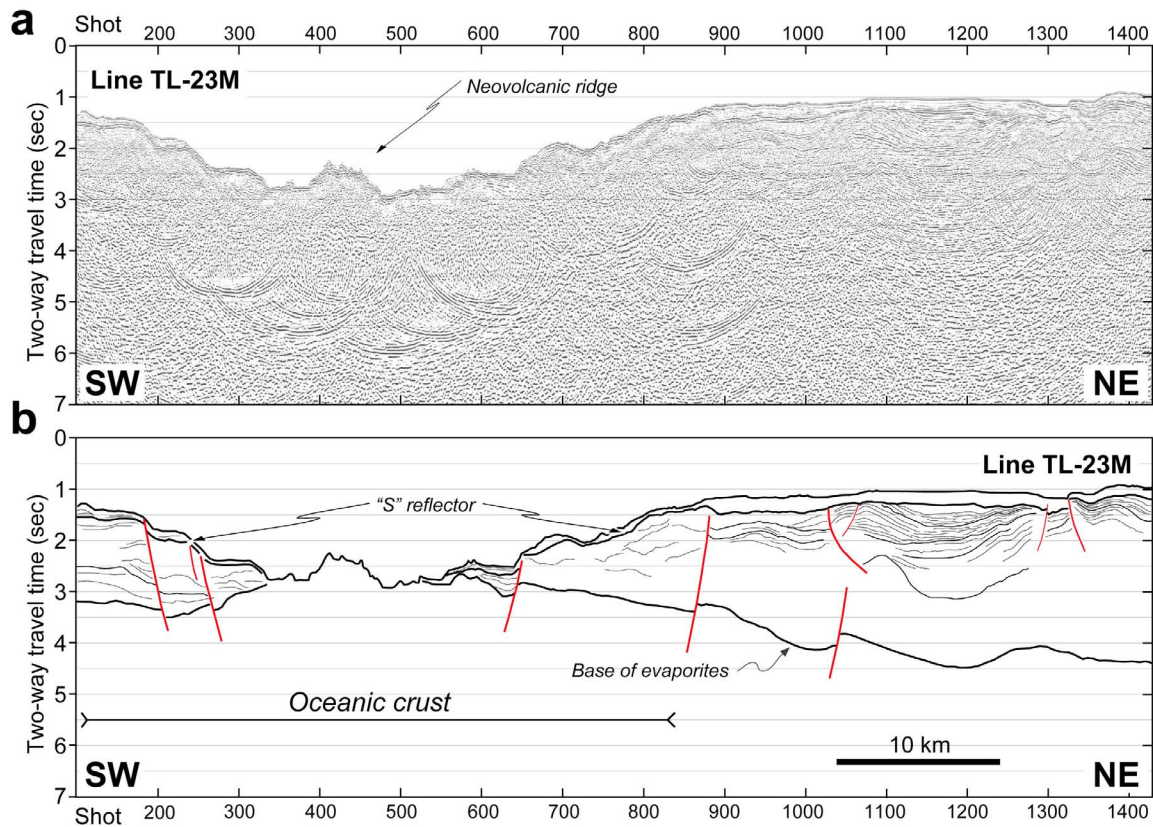
Figure 3. Multichannel seismic line TL-23 M running perpendicular to the axis of the southern Thetis basin. Profile location is indicated as dashed blue line in Figure 1. (a) Finite difference time migrated section. (b) Interpreted line drawing. The extension of the oceanic crust beneath evaporites is inferred from magnetic data.

anomalies were then reduced to the North Pole by phase shifting them of an angle determined from the inclination of the present and the remnant magnetic field directions (Figure 4b). Declinations and inclinations of the present field were estimated from IGRF. Remnant inclination is assumed to be that of an axial geocentric dipole, with the pole coinciding with the present spin axis. Intensity of rock magnetization has been obtained by inversion of reduced-to-the-pole magnetic anomalies using the Fourier method of *Caratori Tontini et al.* [2009] assuming a 1-km thick magnetic layer parallel to the bottom of the evaporite layer (Figure 4c).

2.4. Gravity

[14] Shipboard gravity measurements were corrected and combined with satellite-derived free-air gravity data [*Sandwell and Smith*, 1997], in order to add the ship-gravity high frequency content to the full coverage of satellite data. A total of 10872 shipboard gravity measurements were used from the NGDC database (Figure 5), complemented after

discretization by those in analogue form of *Izzeldin* [1982, 1987]. The overall statistics at 333 crossover points give a mean and standard deviation of 2.5 and 13.1 mGal, respectively. These data were collected over a 20-year period, during which recording instruments and navigation systems greatly improved. In order to integrate these different data sets before merging, the ship gravity for each line was adjusted by applying a series of corrections aimed at reducing the errors at crossover points and at matching the satellite-derived marine gravity field (Figure 5). The unknown parameters of the error model describing changes of systematic error that affects ship gravity data [*Huang et al.*, 1999], were evaluated based on a least squares estimate. After adjustment, the mean and root-mean square (rms) differences between ship and satellite gravity are 0.4 and 5.6 mGal, and the overall cross-track discrepancies are reduced to zero mean and standard deviation of 3.1 mGal, equivalent to an accuracy of 2.2 mGal. The adjusted ship gravity is then blended with satellite-derived gravity to derive a second gravity field (Figure 5b). Different techniques have been developed to combine ship-borne
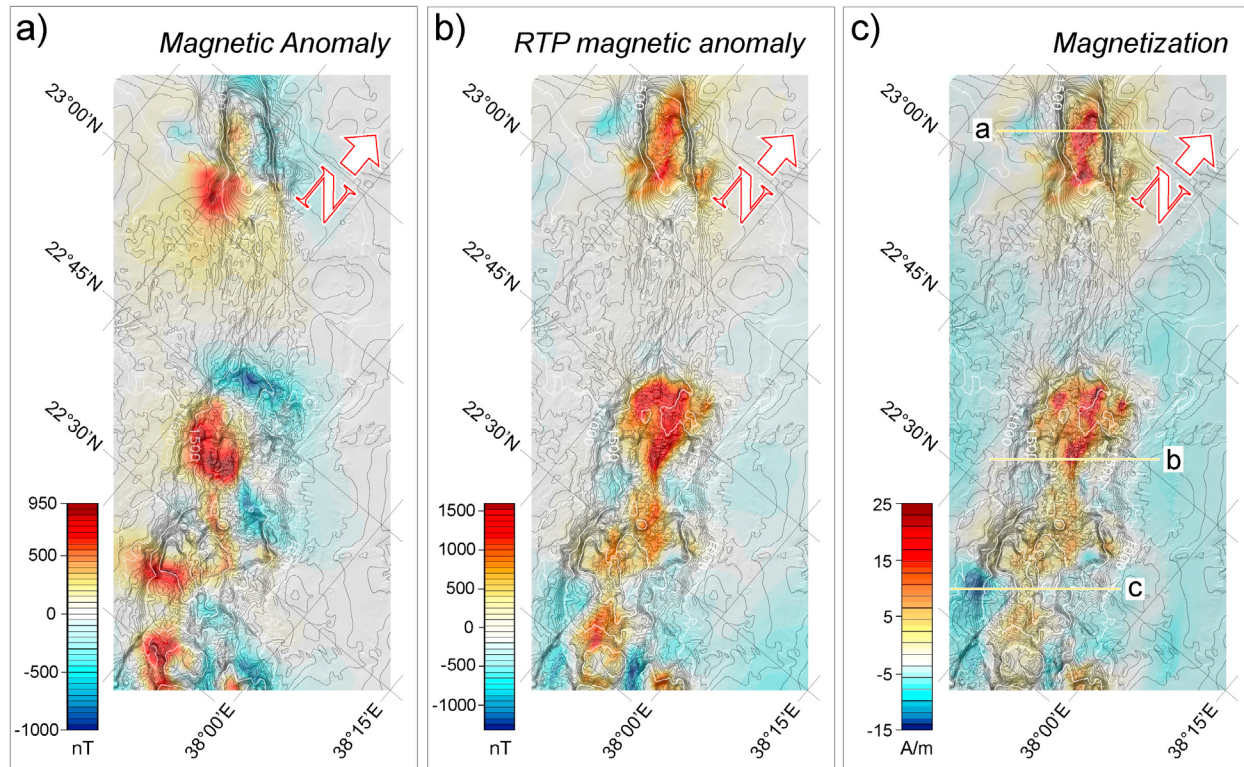
Figure 4. Maps showing magnetic anomalies superimposed on bathymetry. (a) Observed magnetic anomalies. (b) Reduced to the pole magnetic anomaly map. (c) Intensity of rock magnetization obtained by inversion of reduced-to-the-pole magnetic anomalies. Yellow solid lines indicate the location of the across axis geophysical profiles from Thetis and Nereus, shown in Figure 8.

and satellite-derived gravity data, such as least squares collocation [*Hwang and Parsons*, 1995], least squares adjustment in the frequency domain [*Barzaghi et al.*, 1993] and input-output system theory [*Sideris*, 1996; *Li and Sideris*, 1997]. Studies on simulated [*Li and Sideris*, 1997] and real data [*Tziavos et al.*, 1998] have shown that the best results are obtained by the input-output system theory (IOST) method, mainly when the power spectral densities are estimated directly from the data. The use of IOST requires the field of observables be given on the same grid with known error power spectral densities. Ship gravity anomalies were computed on the same grid of satellite-derived global gravity (version 18.1) for the area of interest. We assume gravity anomalies affected by a Gaussian random noise with zero mean and variance of 9.61 mGal² and 25.0 mGal² for ship-board and satellite-derived gravity data, respectively.

2.5. Mantle Bouguer Anomaly

[15] The components of the gravity field due to variations in crustal thickness or crustal and upper mantle density have been calculated by removing the predictable signals produced by density contrast between water, sediments and rocks at the seafloor, and by density variations associated with the temperature field. The contribution of topography, sediments and crust to the local gravity field has been computed from the grids of bathymetry (Figure 2a), post-evaporitic unconsolidated sediments (Figure 2b) and Miocene evaporites (Figure 2c) by a FFT technique based on *Parker* [1973], that uses a series expansion of the Fourier transformed powers of the base of each layer to represent the Fourier transform of the gravity anomaly. The Bouguer correction was obtained by replacing with a layer of mantle material (density of 3330 kg/m³) the water layer (density of 1040 kg/m³), unconsolidated sediments (density of 1900 kg/m³), evaporites (density 2200 kg/m³) and a 5 km constant thickness crust (density of 2670 kg/m³) limited by and parallel to the base of the evaporites. Grids of bathymetry and sediment thickness were produced at 0.15 km of spatial resolution in order to perform up-ward continuation also in the shallowest portion of the Red Sea. Each grid was mirrored to avoid edge effects introduced by the implicit periodic assumption of
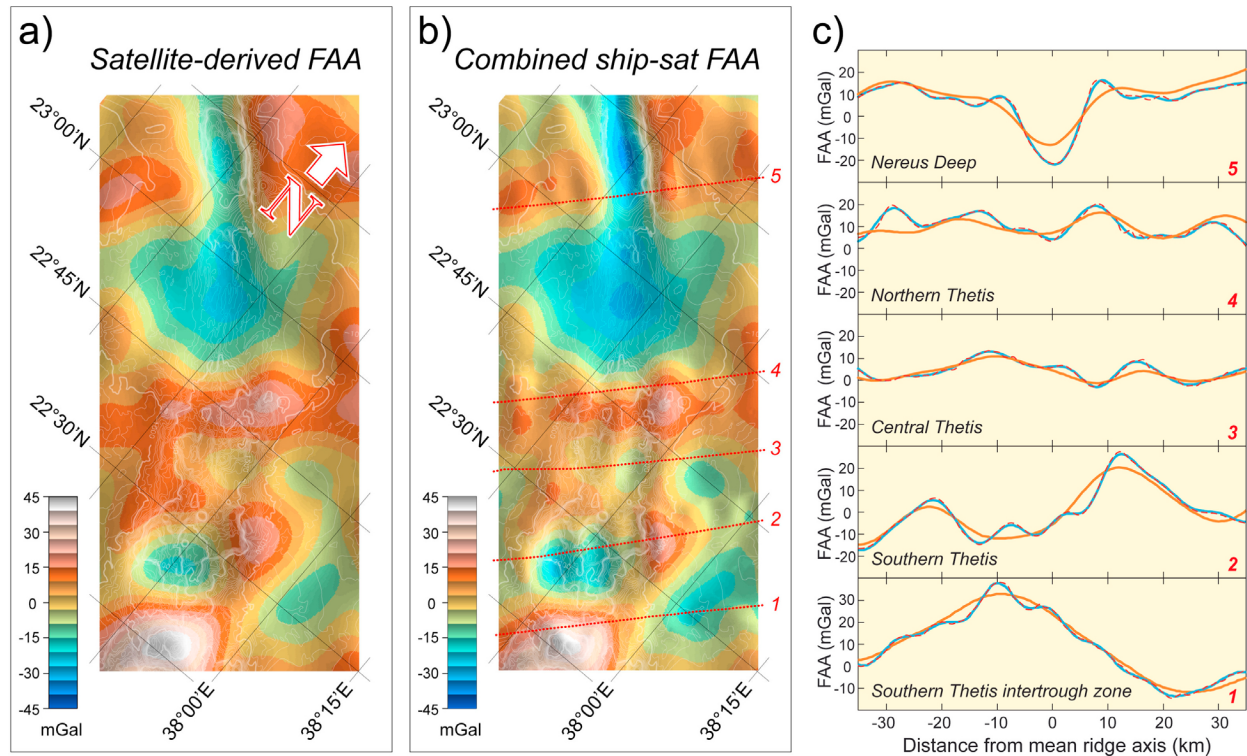
Figure 5. Free air gravity grids. Grid step, 0.3 km. (a) Free air satellite-derived gravity anomalies. (b) Combined ship-borne and satellite-derived gravity field. Dotted red lines indicate locations of across-axis gravity profiles shown in Figure 5c. (c) Across-axis gravity profiles showing differences between satellite-derived and ship-borne free air anomalies. Orange solid line, satellite-derived; red dashed line, shipborne; blue line, combined satellite and ship-borne gravity data according to the IOST method of *Li and Sideris* [1997].

the FFT routine. The predicted gravity contribution of crustal layers, computed at bathymetry grid points, were interpolated onto combined ship-satellite gravity grid points and then subtracted from the corresponding free air anomalies. The new values were then regridded at 0.3 km to obtain the complete mantle Bouguer anomaly (MBA). The zero level is arbitrary and corresponds to the center of the range in anomaly amplitudes (Figure 6a). The calculated MBA, reflecting mostly the thermal and compositional density distribution of the sub-axial mantle, displays minima centered on Thetis and Nereus, separated by a positive anomaly at the intertrough zone (Figure 6a).

[16] Assuming that lateral mantle composition variations, due to phase transitions and mantle chemistry, have wavelengths greater than the study area, the contribution of upper mantle density variations to local gravity can be inferred from the mantle temperature field. The thermal structure beneath a rift axis is related to the temperature at the base of asthenosphere and/or to the mantle upwelling velocity.

2.6. Mantle Thermal Gravity Anomaly and Crustal Thickness

[17] The temperature field has been calculated by the steady state advection-diffusion equation. Mantle temperatures have been computed through the 3D-domain of mantle flow calculations (see Discussion), by the over-relaxation upwind finite difference method described by *Morgan and Forsyth* [1988], using a variable grid spacing ($512 \times 256 \times 101$) with the highest grid resolution (1 km) in the proximity of the plate boundaries.

[18] The predicted thermal mantle contribution (TMGA) to the gravity field was obtained by stacking the gravity signals from all the horizontal layers defined by the finite difference grid. The gravity signal from each layer was computed converting the temperature field into density variations by a thermal expansion coefficient ($3.25 \ 10^{-5}/°C$), then converted into the gravity signal observed at sea level employing a FFT technique. The TMGA is subtracted from the MBA (Figure 6a) to create the residual anomalies (RMBA). The computed
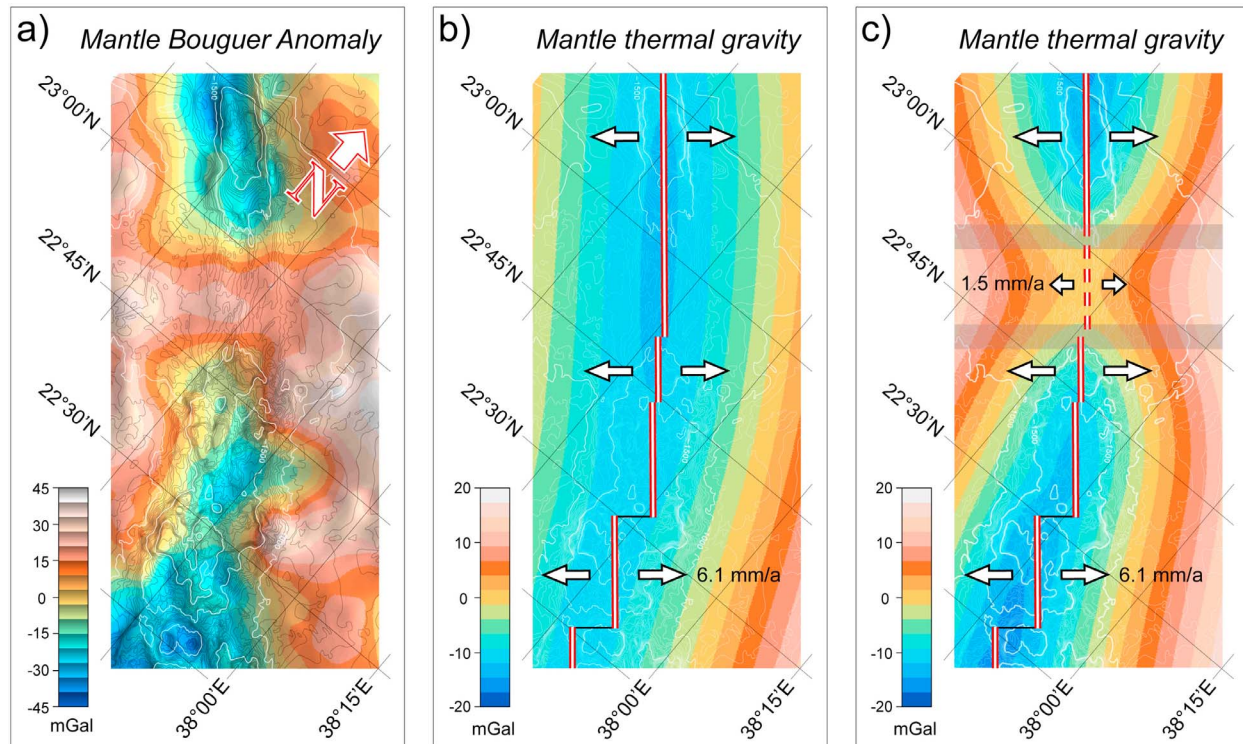
Figure 6. Mantle Bouguer and thermal gravity anomalies. (a) Mantle Bouguer anomaly map generated by subtracting from the computed free-air anomalies the attraction of seafloor topography, sediments and evaporites, and of the crust-mantle interface, assuming 5-km-thick crust. (b) Predicted mantle thermal contribution to the gravity field beneath a plate boundary geometry (Model I) simulating that of the northern central Red Sea, obtained assuming plate-thickening passive mantle flow. (c) Predicted mantle thermal gravity field obtained assuming a reduction in plate separation velocity at the base of lithosphere beneath the Nereus-Thetis intertrough due to lithospheric stretching (Model II), and adopting the mixed thickening-plate driven and upwelling-divergent mantle flow model. Arrow indicates half spreading rate. Gray shaded area represents the sector where spreading velocity is tapered down to a minor fraction of plate separation velocity.

residual low-pass filtered mantle Bouguer anomalies, (wavelengths shorter than 12 km were cut off), were downward continued to a depth of 8 km to infer crustal thickness variations.

2.7. Basalt Chemistry

[19] Dredging of the Tethis and Nereus neovolcanic zones during MR79, MR83 and RS05 expeditions recovered fresh glassy basalts at seven sites. Of the ten sites sampled during cruise RS05 from the along-axis volcanic ridges of Thetis, five recovered basalts and five recovered layered consolidated carbonates rich in pteropods and foraminifera. Two sites sampled during MR79 and MR83 cruises recovered basalts from the southern tip of the Nereus neovolcanic ridge. Major element content of basaltic glasses was determined using a CAMECA SX-100 electron probe using an acceleration voltage

of 15 kV and a beam size of 10 μm at the American Museum of Natural History in New York. The counting times and sample current were of 60 s and 5 nA, respectively for K, Na and Cl, and 30 s and 20 nA for all other elements. Each data point corresponds to the average of at least 5 analyses on 2 or more glass chips (Table 1).

[20] The H_2O content was determined at IGG-CNR in Pavia by secondary ion mass spectrometry (SIMS) with a Cameca IMS 4f ion microprobe following a procedure which involves "energy filtered" secondary ions with emission energies in the range 75–125 eV [Ottolini et al., 1995]. Two reference basaltic glasses were used for calibration: CY82-29-1V (SiO_2 = 49.52 wt%; H_2O = 0.09 wt%) and CLDR01–5V (SiO_2 = 50.43 wt%; H_2O = 0.16 wt%), courtesy of M. Chaussidon, CRPG (Nancy, France). Under these experimental conditions the H background, measured on a sample of

Table 1. Major Element Content and Chemical Parameters Obtained From Basaltic Glasses Sampled Along the Axis of Thetis and Nereus[a]

Sample ID	Latitude	Longitude	Depth	Na_8	Fe_8	$(H_2O)_8$	$(Sm/Yb)_n$	Mg#	SiO_2	TiO_2	Al_2O_3	FeO_T	MnO	MgO	CaO	Na_2O	K_2O	P_2O_5	H_2O
RS05-07-01b	22.4150	37.7695	1732	2.80	10.76	0.24	1.05	0.587	49.71	1.38	14.69	10.97	0.16	7.87	11.25	2.83	0.12	0.15	0.25
RS05-08-01	22.4315	37.7440	1842	2.62	11.18	0.23	1.07	0.590	49.97	1.23	14.98	11.10	0.19	8.05	11.15	2.61	0.11	0.13	0.22
RS05-08-02a	22.4315	37.7440	1842	2.63	11.07	0.23	1.04	0.587	49.71	1.30	15.06	11.11	0.18	7.98	11.16	2.63	0.12	0.14	0.23
RS05-03-02	22.6310	37.6790	1537	2.38	10.09	0.20	1.02	0.469	50.40	2.13	13.54	13.43	0.23	5.99	10.49	2.79	0.18	0.21	0.32
RS05-03-03	22.6310	37.6790	1537	2.41	10.31	0.19	1.03	0.468	50.03	2.17	13.66	13.59	0.22	6.03	10.47	2.82	0.17	0.21	0.31
RS05-03-12a	22.6310	37.6790	1537	2.42	10.27	0.19	1.07	0.462	50.03	2.56	13.63	13.69	0.22	5.95	10.48	2.85	0.18	0.22	0.32
RS05-02-01a	22.6355	37.6240	1690	2.74	11.36	0.22	1.04	0.525	49.38	2.29	14.10	12.80	0.20	7.14	10.55	2.96	0.15	0.18	0.27
RS05-02-01b	22.6355	37.6240	1690	2.66	11.04	0.22	1.04	0.526	49.87	2.21	14.05	12.61	0.20	7.06	10.58	2.88	0.16	0.18	0.27
RS05-10-02a	22.7660	37.5745	1570	2.38	10.01	0.13	0.97	0.591	50.66	1.19	14.65	10.54	0.19	7.68	12.40	2.44	0.07	0.09	0.14
RS05-10-02b	22.7660	37.5745	1570	2.35	10.01	0.13	0.97	0.588	50.63	1.24	14.72	10.60	0.16	7.65	12.48	2.42	0.07	0.09	0.14
MR83-D3-1	23.1112	37.2789	1975	2.12	10.22	0.11	0.76	0.619	49.80	0.89	14.80	9.94	0.18	8.17	12.83	2.10	0.06	0.06	0.10
MR83-D3-B1	23.1112	37.2789	1975	2.15	10.48	0.09	0.84	0.615	50.16	0.88	14.83	10.15	0.16	8.20	12.88	2.11	0.06	0.06	0.09
MR83-D3-3A	23.1112	37.2789	1975	2.18	10.19	0.09	0.78	0.607	50.34	0.86	14.93	9.88	0.18	8.19	13.04	2.15	0.06	0.05	0.10
MR83-D3-3B	23.1112	37.2789	1975	2.17	10.55	0.09	0.78	0.613	49.64	0.89	14.79	10.23	0.16	8.19	12.86	2.14	0.06	0.07	0.08
MR83-D3-4B	23.1112	37.2789	1975	2.26	11.69	0.16	0.83	0.554	49.80	1.41	14.33	12.25	0.18	7.67	10.99	2.32	0.15	0.14	0.18
MR83-D3-4C	23.1112	37.2789	1975	2.12	10.84	0.13	0.84	0.536	50.34	1.44	14.50	12.26	0.19	7.15	11.33	2.26	0.15	0.12	0.16
* MR83-003	23.1112	37.2789	1975	2.41	12.30			0.586	48.88	1.48	14.51	11.70	0.19	8.36	11.54	2.34	0.13	0.02	
* MR83-003-1	23.1112	37.2789	1975	2.06	9.96			0.617	49.94	0.90	15.21	9.89		8.04	13.21	2.05	0.08	0.08	
* MR83-003-4A	23.1112	37.2789	1975	2.15	10.97			0.554	49.82	1.45	14.85	11.89		7.45	11.46	2.24	0.17	0.12	
* MR83-003-6A	23.1112	37.2789	1975	2.16	11.05			0.554	49.63	1.42	14.96	11.93		7.47	11.49	2.25	0.16	0.13	
* MR79-034-A	23.1973	37.2825	1749	2.41	12.32			0.578	49.40	1.52	14.58	11.92	0.15	8.24	11.56	2.36	0.11	0.12	
MR79-34-11A	23.1973	37.2825	1749	2.38	10.22	0.14	0.84	0.591	50.55	1.05	14.39	10.62	0.18	7.76	12.42	2.43	0.10	0.08	0.15

[a] Asterisk marks samples from *Antonini et al.* [1998].

Table 2. Trace Element Abundances of Basaltic Glasses From Thetis and Nereus[a]

Sample ID	Sc	Ti	V	Cr	Rb	Sr	Y	Zr	Nb	Cs	Ba	La	Ce	Nd	Sm	Eu	Gd	Dy	Er	Yb	Hf
RS05-07-01b	42.35	9831.90	340.80	320.95	4.47	102.10	38.35	102.45	3.20	0.05	19.07	3.50	11.71	11.06	3.97	1.51	5.43	6.72	4.23	4.18	3.10
RS05-08-01	42.72	9381.00	325.65	351.00	4.42	101.35	37.40	96.20	2.81	0.03	18.27	3.30	10.67	10.25	3.75	1.32	5.11	6.32	4.00	3.88	2.72
RS05-08-02a	41.60	9528.70	340.80	352.05	3.70	105.60	35.70	98.85	3.27	0.03	20.95	3.26	10.83	9.76	3.73	1.44	5.26	6.20	3.99	3.97	2.95
RS05-03-02	48.73	13952.00	444.50	101.00	6.40	103.15	52.25	138.30	5.21	0.04	29.63	5.29	16.91	14.86	5.15	1.85	7.04	8.81	5.64	5.55	4.09
RS05-03-03	48.15	13864.50	441.50	100.50	6.47	103.30	52.30	139.30	5.08	0.02	29.89	5.23	17.02	14.98	5.19	1.88	6.91	8.33	5.36	5.56	4.15
RS05-03-12a	48.10	14024.00	446.00	98.50	6.20	102.16	51.51	137.99	4.99	0.02	30.03	5.26	17.18	15.33	5.22	1.86	6.94	8.54	5.45	5.38	4.10
RS05-02-01a	44.36	12514.67	397.67	232.67	5.32	105.61	48.41	128.61	4.43	0.03	24.74	4.68	15.27	13.82	4.82	1.73	6.54	8.03	5.20	5.13	3.96
RS05-02-01b	44.89	12539.50	397.00	239.00	5.58	104.25	48.80	129.00	4.54	0.02	24.91	4.79	15.57	14.40	4.96	1.80	6.63	8.14	5.21	5.26	3.88
RS05-10-02a	44.80	6963.55	311.10	164.65	3.90	81.15	27.65	58.35	1.86	0.00	13.25	2.02	6.61	6.49	2.68	1.09	4.02	4.84	3.01	3.04	1.91
RS05-10-02b	47.95	7152.00	322.00	172.65	4.00	89.95	28.25	59.75	2.15	0.00	14.05	2.10	6.87	7.05	2.83	1.20	4.21	5.26	3.21	3.22	2.07
MR83-D3-1	42.12	5333.19	307.73	414.86	2.72	47.85	24.88	33.09	1.37	0.01	11.26	1.24	3.85	4.15	1.90	0.81	3.07	4.27	2.67	2.77	
MR83-D3-B1	42.96	5304.93	305.75	402.62	2.48	47.69	25.92	33.52	1.32	0.02	11.68	1.22	3.81	4.27	2.09	0.76	3.15	4.30	2.81	2.77	
MR83-D3-3A	45.99	5383.25	298.54	433.94	2.45	46.85	26.40	33.45	1.30	0.02	10.84	1.19	4.01	4.46	2.01	0.85	3.65	4.91	3.15	2.84	
MR83-D3-3B	46.18	5347.53	297.10	426.66	2.20	46.51	26.56	33.58	1.25	0.01	11.07	1.19	4.03	4.49	1.97	0.86	3.48	4.51	3.05	2.81	
MR83-D3-4B	40.47	8805.60	381.32	288.75	5.40	60.17	38.76	70.40	3.80	0.02	29.56	2.99	9.14	8.18	3.12	1.27	4.71	6.28	4.32	4.14	
MR83-D3-4C	38.53	8634.63	380.79	269.93	5.57	60.97	37.51	72.30	4.00	0.06	30.40	3.02	8.97	8.01	3.17	1.28	4.77	6.23	4.28	4.17	
MR79-34-11A	42.89	6291.99	341.89	141.43	2.87	68.23	28.44	45.25	2.39	0.02	17.22	2.25	6.20	5.42	2.29	0.95	3.66	4.96	3.09	3.04	

[a]Concentrations reported in ppm wt.

quartz, is typically 0.009 wt% H_2O. The values for H_2O in Table 1 are the average of 2–6 measurements. The accuracy of analysis is estimated to be <15% relative.

[21] Trace elements were determined with the Pavia ion microprobe (Table 2). The values in Table 2 are the average of two measurements. An optimized energy filtering technique was applied to remove complex molecular interferences in the secondary ion mass spectrum. Light REE-rich basalts were analyzed applying a deconvolution filter to the secondary ion REE mass spectrum in order to reduce residual oxide interferences (i.e., BaO on Eu, CeO, NdO on Gd, GdO on Yb, and EuO on Er). Precision of the measure is on the order of 10% relative for REE concentrations in the range 0.1–0.7 ppm. Below 0.1 ppm precision is mainly limited by (Poisson) counting statistics and falls to ~30% relative. Accuracy is on the same order. The experimental conditions involved a 9.5 nA, ^{16}O-primary ion beam accelerated through ~12.5 kV and focused into a spot 10–15 μm in diameter, and energy-filtered (75–125 eV) positive secondary ions detected under an ion image field of 25 μm [*Bottazzi et al.*, 1994].

[22] Low pressure fractionation influences MORB composition, thus in order to correct for the effects of differentiation, we calculated Na_8, Fe_8 and $(H_2O)_8$, i.e., Na_2O, FeO and H_2O normalized to 8 wt% MgO [*Klein and Langmuir*, 1987; *Plank and Langmuir*, 1992; *Taylor and Martinez*, 2003], assuming olivine-plagioclase-clinopyroxene fractionation. In order to limit possible errors introduced by this correction, we used only analyses with 5.5–8.5% MgO (Table 1).

3. Field results

[23] A nearly complete multibeam coverage revealed that the Thetis and Nereus rift valleys, emplaced within the sedimentary-evaporitic sequence ubiquitous in the Red Sea, are separated by a slightly depressed "inter-trough zone" (Figure 2).

3.1. Thetis Deep

[24] The Thetis, 65-km-long, ~2200 m deep axial valley, is made by the coalescence of three slightly offset sub-basins (southern, central and northern) that become shallower and narrower from south to north (Figure 2a). Each of the three basins is characterized by a linear axial volcanic ridge associated with a strong magnetic anomaly, as well as by scattered small (few hundred meters high) central
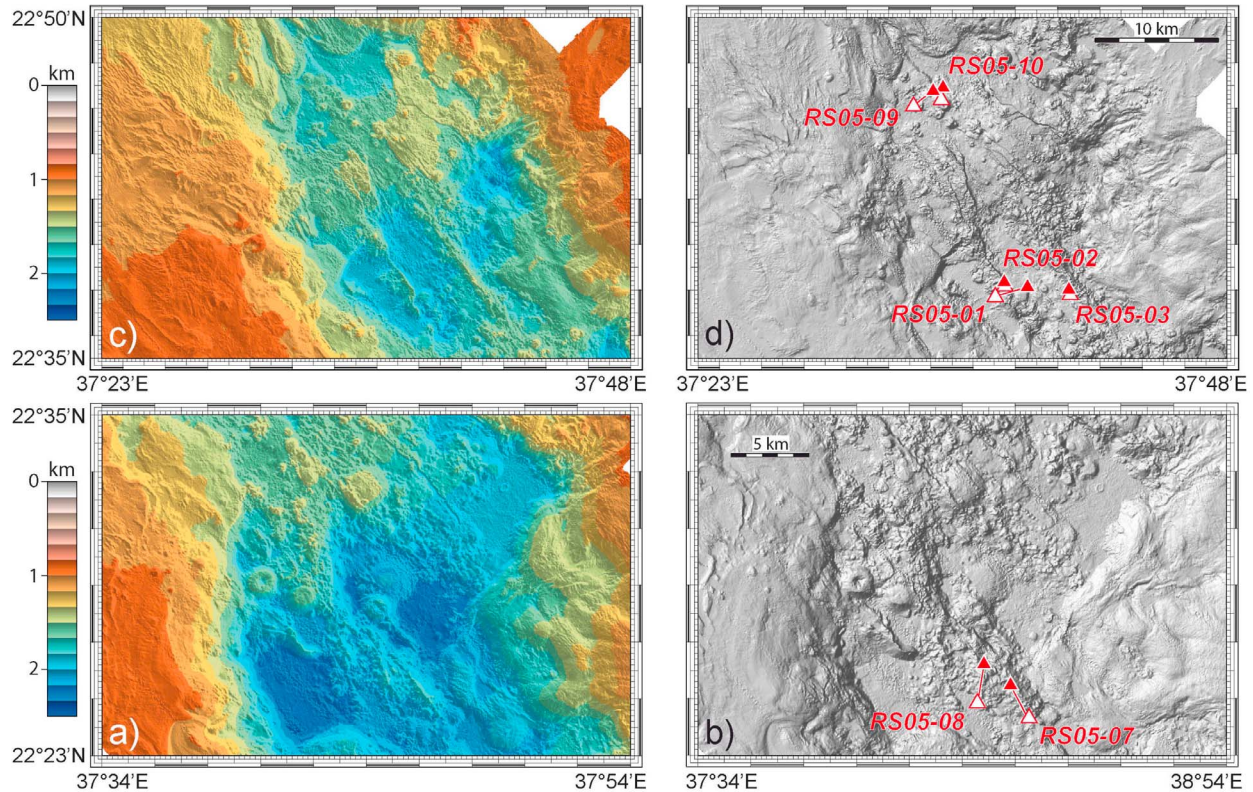
Figure 7. Close-up of the central and northern Thetis basins. (a, c) Shaded relief image with color coded depths and source of light from NE. (b, d) Shaded relief map. Illumination is from NW with an elevation of 45° above the horizon. White and red triangles mark dredge sampling profiles.

volcanoes. This pattern is similar to that observed in the northern Afar Rift, that portion of the Red Sea Rift system that, although mostly below sea level, is on dry land in Eritrea/Ethiopia [*Barberi and Varet*, 1977; *Ebinger et al.*, 2010]. Each of the three sub-basins is separated by small inter-trough zones with no evidence of left-lateral shear deformation. The floor of the Tethis valley is generally sediment-free or with sediment thickness below the acoustic resolution of our seismic reflection system. The >1 km high valley walls show step-like morphology, expression of extensional normal faults partly smoothed by downslope sliding of Miocene evaporites [*Mitchell et al.*, 2010]. Tectonic features lie frequently parallel or perpendicular to the seafloor gradient, suggesting that gravity is an important factor in their origin.

[25] The Thetis "southern sub-basin" axial neo-volcanic ridge shows high acoustic backscatter and crustal magnetization. It is sharp-crested, ~20 km long, ~4 km wide and ~400 m high, and is covered by hummocky terrains made up by coalescence of several volcanic centers ranging from steep-sided cones to low domes. The magma is probably

generated from a central location below the segment, and ascends along axial faults. Fissure eruptions are important in constructing the ridge, resulting in alignments of edifices along the regional tectonic trend. The valley floor flanking the neovolcanic zone displays smooth terrains consisting mostly of flat-lying lava fields, probably basaltic "sheet flows" generated by eruptions of voluminous, high temperature, low viscosity melts (Figures 7a and 7b).

[26] Two negative symmetric magnetic anomalies flank the axial anomaly (c1n) in the southernmost part of the Thetis southern sub-basin, suggesting an initial emplacement of oceanic crust as early as 2.2 Ma, with an average full spreading rate of ~16 mm/a, ranging from 23 mm/a during Matuyama (2.59 ÷ 0.78 Ma) down to 8 mm/a during Brunhes (<0.78 Ma) (Figure 8c). Intervals of higher spreading rates correspond to areas of thicker crust (Figure 8c). Moving north within the southern sub-basin, the neo-volcanic ridge narrows and is flanked by several small individual volcanic cones and by few large flat-top and summit caldera central volcanoes (~300 m high and ~2 km diameter). The negative magnetic anomalies flanking the axial
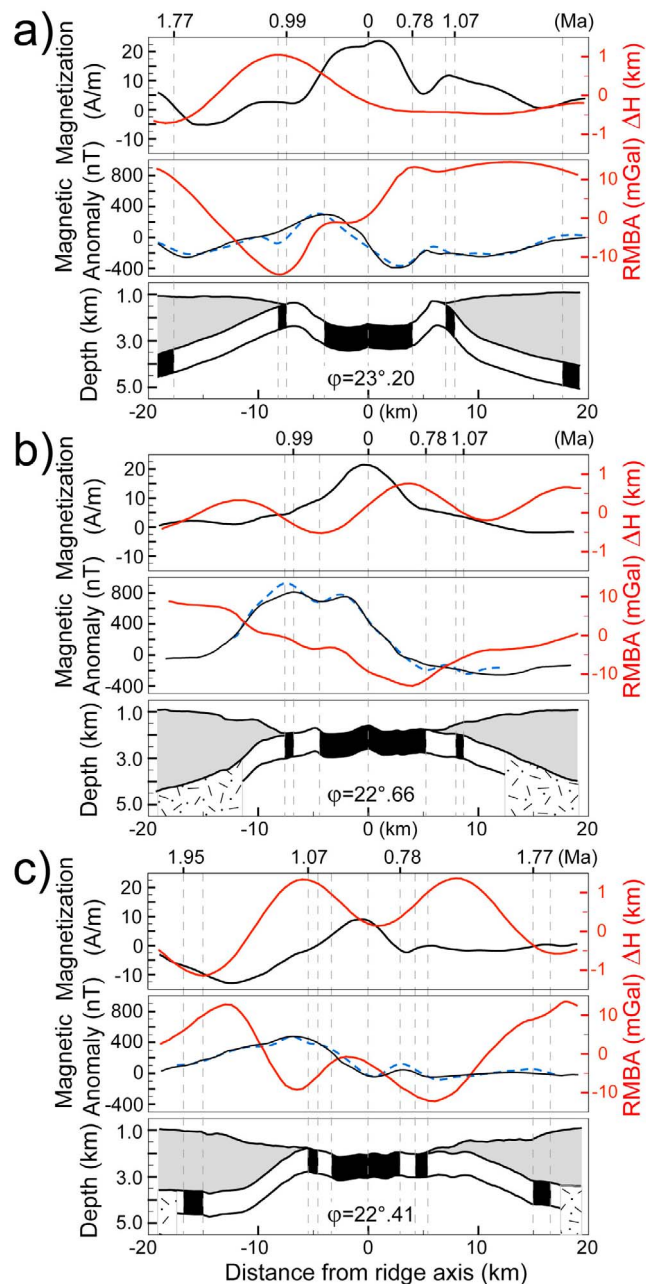
Figure 8. Gravity and magnetic profiles across mid-segment points of (a) Nereus, (b) Thetis central and (c) southern sub-basins. φ, latitude of each profile at ridge axis. Bottom plot in each set: geological model. Gray shaded area: sediment and evaporite layer. Black and white stripes: normal and reverse geomagnetic events. Hatch pattern: transitional crust. Geomagnetic scale from *Cande and Kent* [1995]. Middle plot in each set: observed (black solid line) and synthetic (blue dashed line) magnetic anomalies; and residual mantle Bouguer anomaly (red solid line). Top plot in each set: inferred variations of rock magnetization (black solid line) and crustal thickness (red solid line).

anomaly disappear in this sector, implying a younger initial emplacement of oceanic crust (Figure 4). The valley floor displays a second en-echelon axial volcanic ridge displaced eastward by ~10 km and lined up with the axial neovolcanic zone of the central sub-basin to the north. This pattern suggests over-shooting of multiple dike intrusions from mid-

segment melt injections, that maintains along-axis segmentation during early stages of ocean basin formation [*Wright et al.*, 2006].

[27] A large (~10 km diameter, ~1 km high) circular relief rises at the southern edge of the Thetis basin. It is affected by extensional faults oriented in
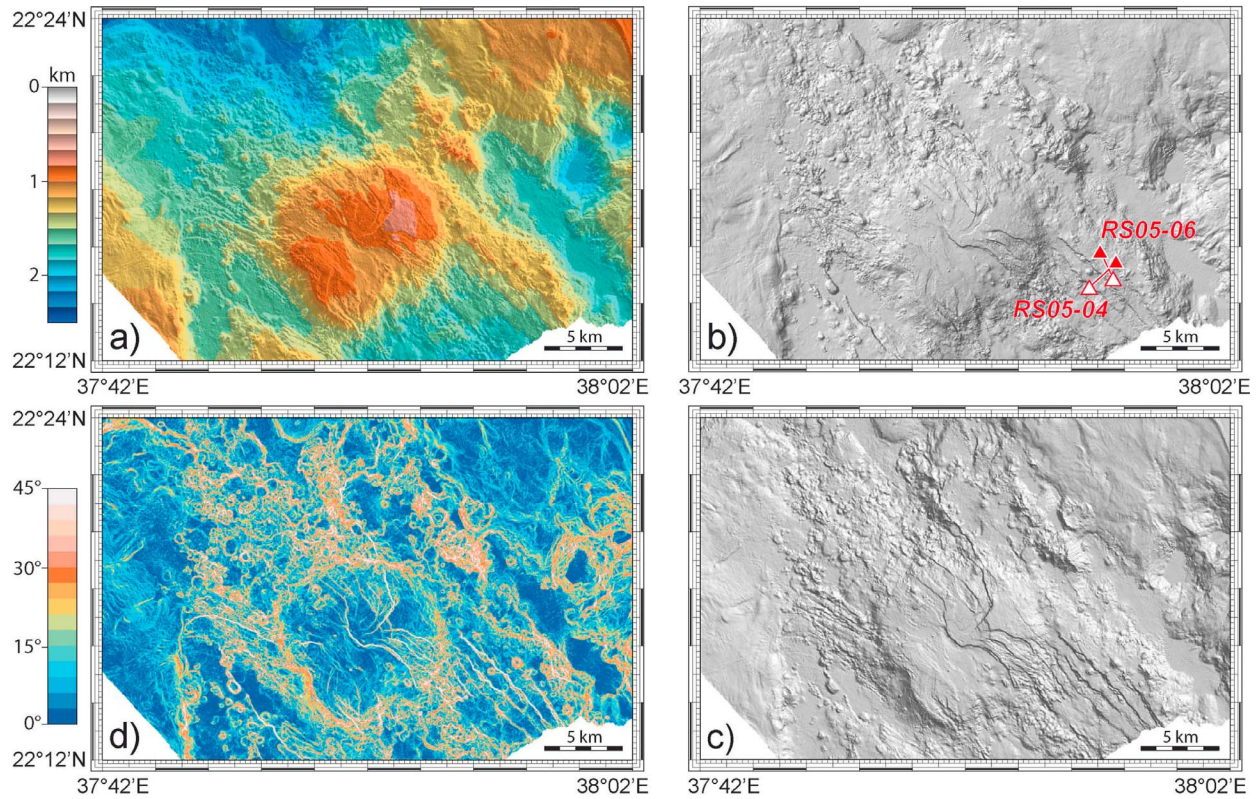
Figure 9. Close-up of the Thetis southern edge. (a) Shaded relief image with color coded depths and source of light from NE. (b) Shaded relief map. Illumination is from NW and symbols as in Figure 7. (c) Map of topographic slopes. Color bar is in degrees of topographic slopes. The topographic gradient was computed along eight different direction at each node of the bathymetric grid. The plotted slope corresponds to the maximum gradient. (d) Shaded relief map with illumination from NE.

a Red Sea direction (Figure 9). This, a low intensity of magnetization and a relatively thick crust (Figure 10) suggest it is not a young "oceanic" basaltic construction. It could be a serpentinized massif of mantle-derived peridotites [*Sibuet et al.*, 2007]. However, exposed mantle massifs at mid-ocean ridges show a very smooth morphology [*Cannat et al.*, 2009]. Instead, this sub-circular structure shows very steep flanks and a flat summit cut by several sub-vertical normal faults, implying brittle rheology. Remnants of continental crust have been described from the West-Iberian margin [*Manatschal et al.*, 2001], suggesting that the feature at the southern end of Thetis may be the remnant of a Pan African batholith similar to those observed along ancient structural lineaments in southern Egypt and Sudan [*Dixon et al.*, 1987]. Remnants of continental crust, acting as "locked zones" [*Courtillot*, 1982], may be present in the inter-trough zones separating Thetis from the next oceanic segments to the South (Hadarba Deep) and to the North (Nereus Deep) (Figure 1).

[28] The Thetis "central sub-basin," in addition to scattered small volcanoes, has a strongly magnetic axial neo-volcanic zone (10 km long, 2 km wide and 300 m high), that grows within a rift valley flanked by a pair of master faults, 10 km apart and with large throws accommodating a vertical displacement of ~300–500 m. The axial volcanic ridge and the shoulders of axial valley master faults are covered by volcanic hummocks, whereas the valley floor outside these regions displays flat-lying sheet lava flows (Figures 7c and 7d). The axial volcanic ridge is flanked by narrow symmetrical negative magnetic anomalies only, suggesting initial emplacement of oceanic crust roughly 1.6 Ma (Figure 8b), with an average spreading rate of 15 mm/a, affected by a slight asymmetry (~10% faster to the E).

[29] The Thetis "northern sub-basin" lacks a clearly defined linear neovolcanic zone although it displays a strong central magnetization, suggesting a recent (<0.78 Ma) initial emplacement of oceanic crust. In the southern portion of the sub-basin, an
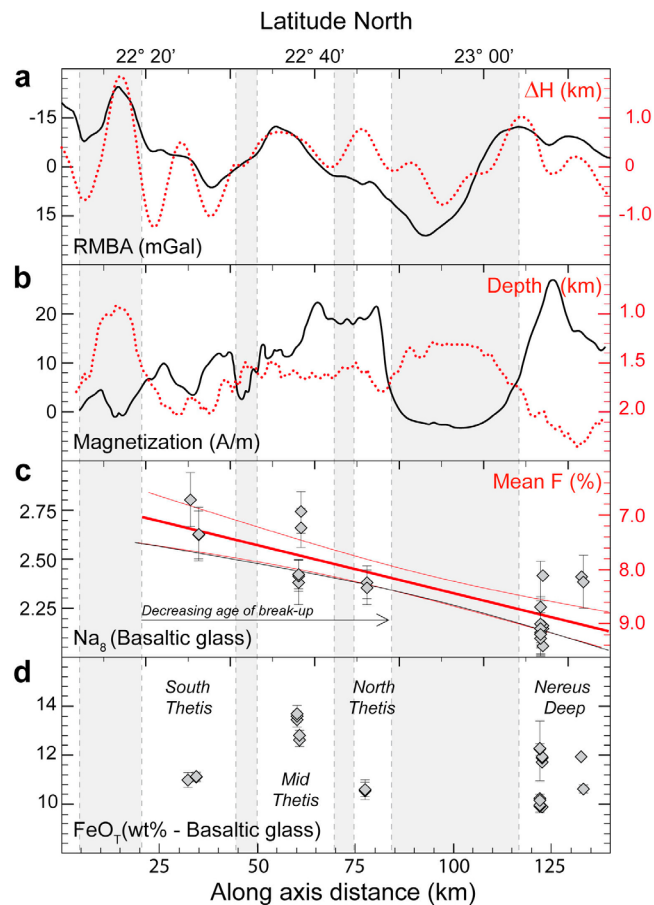
Figure 10. Along axis variations of crustal thickness, rock magnetization, degree of melting (from basalt Na_8) and basalt Fe content. Error bars indicate 2σ standard deviation of the mean. Profile location is in Figure 1 (red solid line). (a) RMBA (black solid line) and inferred variations of crustal thickness ΔH (red dotted line). (b) Intensity of rock magnetization (black solid line) and seafloor topography (red dotted line). (c) Na_8 of basaltic glasses and mantle degree of melting estimated from Na_8 assuming a pure-fractional melting regime and complete melt extraction [*Ligi et al.*, 2005]. Na_2O normalized to 8 wt% MgO, according to *Plank and Langmuir* [1992]. Thick red line is a linear regression showing increasing degree of mantle melting with decreasing age of breakup (thin red lines: 95% confidence intervals). (d) Total FeO of basaltic glasses.

embryonic volcanic axial ridge is growing from coalescence of central volcanoes aligned along axial normal faults. In contrast, the northern portion of the axial region is characterized by a single 150 m-throw NE-dipping normal fault. Outside the axial region, flat morphology and young sediments (<23 ka) overlying basalts, with thickness <10 m [*Scholten et al.*, 1991; *Mitchell et al.*, 2011], suggest a valley floor covered mostly by smooth lava flows (Figures 7c and 7d). The geochemistry of the sediments indicates hydrothermal activity varying through time [*Pierret et al.*, 2010].

[30] This pattern implies a south to north time progression of the initial emplacement of oceanic crust within the Thetis system, with a propagation rate of roughly 30 mm/a, significantly faster than the spreading rate. Magnetic profiles from the northern part of Hadarba Deep (the "oceanic" segment immediately to the south of Thetis), indicate an initial oceanic accretion at ~3 Ma [*Izzeldin*, 1987; *Chu and Gordon*, 1998], confirming its south to north progression.

3.2. Nereus Deep

[31] The Red Sea northernmost "oceanic" segment is Nereus Deep, a ~50 km long, ~2500 m deep axial rift valley (Figure 2a) flanked by >1 km asymmetric walls (eastern side higher and steeper) with step-like morphology due to normal faults partly masked by "salt tectonics" at segment ends [*Ligi et al.*, 2011]. A ~250 m high neo-volcanic axial ridge exposing fresh oceanic-type basalts
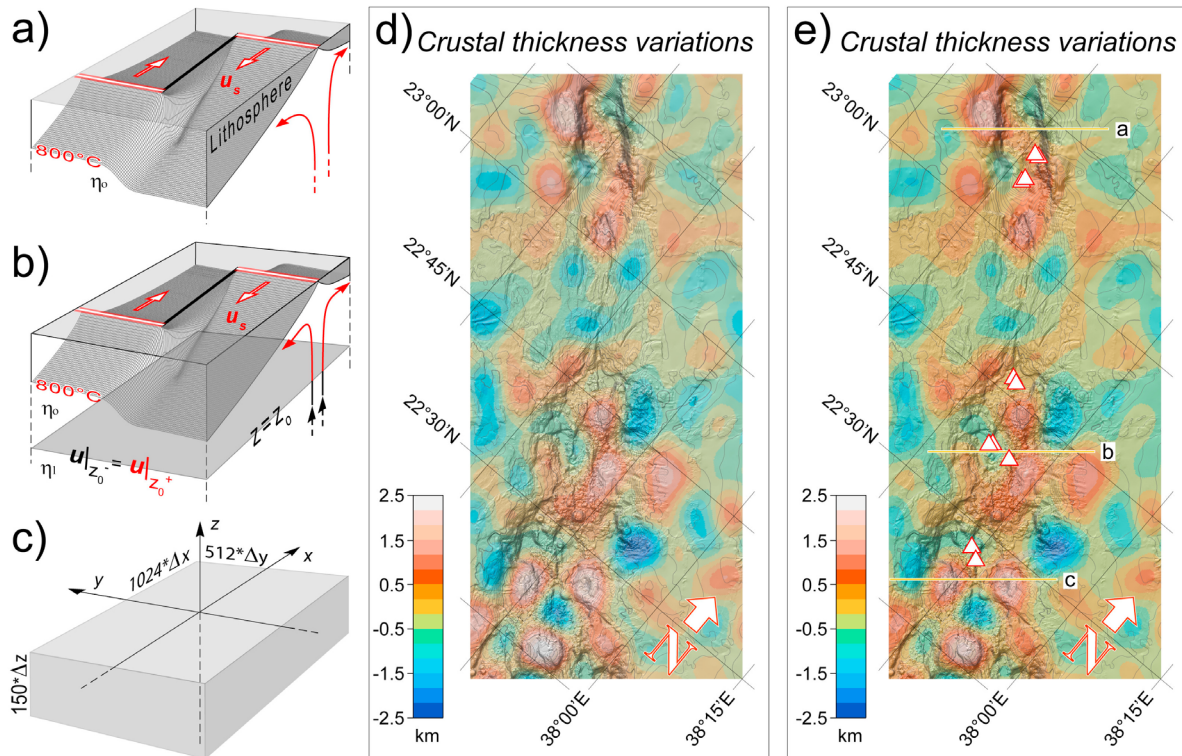
Figure 11. Mantle flow model geometries and boundary conditions. (a) Thickening-plate passive flow model, where the gray shaded surface indicates the base of the lithosphere assumed to correspond in our calculations to the depth of the 800°C isotherm. An incompressible and isoviscous (η_0) mantle flows within the half-space by motion of overlying rigid plates moving apart with velocity $\mathbf{u}_s$. (b) Mixed thickening-plate driven and upwelling-divergent mantle flow model to simulate a flow that is passive within an upper layer and active below. Boundary conditions for the lower limit z_0 of the upper layer are the mantle velocities from an upwelling divergent flow in the half-space below. (c) Cartesian reference system used as vector basis, and geometry and scale of the model. Flow velocity grid step size is $\Delta x = \Delta y = \Delta z = 1$ km. (d, e) Crustal thickness variations with respect to the reference 5-km-thick crust, obtained after downward continuation to a depth of 8 km of the RMBA computed by subtracting from the MBA in Figure 6a, the TGMA in Figures 6b and 6c, respectively. Note that although crustal thickness values are affected by the thermal correction we used, the pattern of crustal variations is approximately the same regardless of mantle flow models we adopted to calculate the mantle thermal structure. White filled triangles show the location of rock samples from Table 1. Yellow solid lines indicate the location of the across axis geophysical profiles from Thetis and Nereus, shown in Figure 8.

dissects the 12 km wide valley floor [*Bonatti et al.*, 1984]. A strong axial magnetic anomaly is flanked at mid-segment point by symmetrical reversed anomalies (Matuyama chron), that vanish toward segment ends, suggesting that the Nereus "oceanic" cell started about ∼2 Ma (Figure 8a). Crustal thickness is at a maximum in the areas of reversed magnetization (Figures 4c and 11); moving southeastward the maximum thickness shifts toward the axis of the basin. Average full spreading rate is 20 mm/a, with a maximum of 26 mm/a during Matuyama, slowing down to 10 mm/a during Brunhes. Axial propagation is suggested by younger seafloor and higher zero-age melt production toward the segment tips (Figures 4c, 10c, and 11).

3.3. Thetis–Nereus Intertrough Zone

[32] A ∼35 km long, broad and gentle depression, carpeted by sediments and devoid of volcanism and linear magnetic anomalies separates the Thetis and Nereus segments (Figure 2). The inter-trough seafloor is affected by curvilinear ridge-trough topography aligned in a Red Sea direction (Figure 2a). Seismic reflection profiles suggest they are due to folding of the sedimentary sequence, caused by evaporite flowage toward the rift axis, that carried passively the overlying hemipelagic layer [*Mitchell et al.*, 2010]. The axial depression broadens in the inter-trough zone relative to the "oceanic" segments: the 1000 m isobath encloses an axial area ∼80 km wide at the intertrough zone, but only

40 and 30 km wide at Nereus and Thetis, respectively (Figure 1). This pattern indicates that deformation becomes focused in a narrow axial zone as soon as oceanic accretion starts. In the Afar Depression extension is dominated by diking with density of dike-induced faulting increasing toward the rift axis. The majority of plate opening in this zone of incipient rupture is achieved by magma intrusions [*Ebinger et al.*, 2010; *Keir et al.*, 2011; *Rychert et al.*, 2012]. By analogy, we speculate that the Thetis-Nereus inter-trough zone consists of stretched-thinned continental crust, injected by diffuse basaltic intrusions, capped by Miocene evaporitic and Plio-Quaternary biogenic deposits (Figure 2).

4. Discussion

[33] Adiabatic decompression melting, commonly accepted beneath mature mid-ocean ridges, may be difficult to apply beneath the Red Sea, where models predict that cool continental lithosphere and slow continental rifting (8–16 mm/a) lead to negligible melt production [*Schmeling*, 2010; *Corti et al.*, 2007]. Given the low plate separation velocity of ~12.2 mm/a in the central Red Sea, we would expect a magma starved rift, with a rift-to-drift transition marked by exhumed mantle and initial alkaline magmatism [*Jagoutz et al.*, 2007]. Exposed peridotites in magma poor rift related areas such as Iberia-Newfoundland or Alps show a complex interaction between melt and lithospheric mantle with widespread occurrence of refertilized plagioclase peridotites [*Müntener et al.*, 2004; *Le Roux et al.*, 2007; *Müntener et al.*, 2010]. However, our geochemical data show a rift-to-drift transition marked by magmatic activity with typical MORB signature and relatively high degree of mantle melting, with no contamination by continental lithosphere (Tables 1 and 2). Most of the observed geochemical variability of Thetis and Nereus basaltic glasses can be explained by varying mean degree and mean pressure of melting from a source having Depleted MORB Mantle (DMM) composition [*Workman and Hart*, 2005]. This is consistent with a model where depth-dependent extension, due to decoupling between the upper and lower lithosphere, results in mantle-lithosphere necking breakup before crustal-necking breakup [*Kuznir and Karner*, 2007; *Huismans and Beaumont*, 2011]. Thus, lower crust and mantle lithosphere have been replaced beneath the axial part of the Central Red Sea by upwelling asthenosphere before separation of the Nubian and Arabian plates, suggesting

melting and mantle flow models similar to those adopted for mature mid-ocean ridges.

4.1. Models of Mantle Flow

[34] Fluid-mechanical calculations on mantle flow and melting at spreading centers, produce models where either mantle upwelling and melting are caused solely by plate separation at ridge axis (passive model), or where a dynamic component of mantle flow is required (dynamic model), driven by thermal and compositional buoyancy [*Forsyth*, 1992]. In passive models the mantle flow pattern is shaped dominantly by viscous drag from rigid plates moving apart, with melt generated in a broad upwelling region. Mantle flow velocity is affected by plate geometry close to ridge axis, and the upwelling velocity can exceed the half spreading rate when the plate thickens rapidly with distance from ridge axis [*Reid and Jackson*, 1981; *Morgan and Forsyth*, 1988; *Blackman and Forsyth*, 1992; *Shen and Forsyth*, 1992]. In dynamic flow models, with buoyancy forces and low viscosities in the melting region, the mantle upwells close to the spreading axis in a region only a few kilometers wide; upwelling is much faster than half spreading rate, and melt moves vertically primarily due to its buoyancy [*Buck and Su*, 1989; *Scott and Stevenson*, 1989; *Sotin and Parmentier*, 1989].

[35] Partial melting of the subridge upwelling mantle may induce significant density and viscosity changes, triggering dynamic upwelling due to buoyancy of the retained melt and to reduced density of the residual depleted mantle. However, melt retention of at least several percent is required to provide buoyancy and to reduce viscosity [*Cordery and Morgan*, 1992, 1993]. In addition, melting leads to rapid dehydration of the mantle increasing the viscosity of the residue by up to two orders of magnitude [*Hirth and Kohlstedt*, 1996; *Braun et al.*, 2000]. On the other hand, small amounts of interstitial melt can favor grain boundary sliding reducing the effective viscosity. Short-term temporal variations of mantle upwelling below a segment of the Mid Atlantic Ridge have been ascribed to active components due to non-uniform mantle rheology, with a sub-ridge low-viscosity zone between layers with higher viscosity due to loss of H_2O [*Bonatti et al.*, 2003; *Cipriani et al.*, 2009]. The increased viscosity in the upper part of the melting region (where dry melting occurs) induced by dehydration, limits buoyant upwelling; as a consequence, solid flow within the upper layer is mostly driven by plate separation. Buoyancy-

Table 3. Testing Model Parameters[a]

Constraining Model Parameters	Flow Model	H_2O wt%	T_p (°C)	V_s (mm/a) − V_z^0/V_x^0	Plate Boundaries
Water content in the upper mantle	Passive Flow	0.005 ÷ 0.025 (0.005)	1330 ÷ 1430 (10)	6.1	Model I
Thermal mantle gravity anomaly	Passive Flow	0.02	1330 ÷ 1430 (10)	6.1	Model I and II
Melting parameters and melt composition	Passive Flow	0.02	1330 ÷ 1430 (10)	6.1	Model I
Reference mantle potential temperature	Passive Flow	0.02	1300 ÷ 1450 (25)	3.9 ÷ 75.0	Global Ridge System
Thermal mantle gravity anomaly	Dynamic Flow	0.02	1350	$2/\pi$, 1 ÷ 4.5 (0.5)	Model I and II
Melting parameters and melt composition	Dynamic Flow	0.02	1350	$2/\pi$, 1 ÷ 4.5 (0.5)	Model I

[a]T_p is mantle potential temperature at the reference depth of 150 km (bottom of the model). V_s is the half spreading rate used in passive flows; $V_z^0(x = 0, z)$ and $V_x^0(x, z = 0)$ are the upwelling and the half plate separation velocity, respectively, used in the dynamic flows, (V_x^0 is assumed equal to V_s = 6.1 mm/a). Number in parentheses indicates step of parameter variation.

driven convection, confined in the lower part of the melting region, has been suggested as a possible mechanism for magmatic segmentation of slow spreading ridges [*Choblet and Parmentier*, 2001]. At the rifting stage, the solid mantle can upwell into a series of closely spaced cells, with their spacing depending on the viscosity structure of the rising mantle [*Bonatti*, 1985; *Choblet and Parmentier*, 2001; *Wang et al.*, 2009].

[36] We predicted the mantle thermal structure, adopting a number of different mantle flow models (Table 3): thin and thickening plate passive flow; and a modified three-dimensional upwelling divergent flow [*Kuznir and Karner*, 2007] to simulate mixed active-passive flows. We modeled the flow beneath an accretionary plate boundary geometry that duplicates the central Red Sea rift, in a computational frame 1024 × 512 km wide and 150 km deep (1 × 1 km spaced grid points for each 1 km depth increment) (Figure 11). Two different plate boundary geometries were tested (model I and II): one with constant plate separation velocity of 12.2 mm/a [*Chu and Gordon*, 1998] (Figure 6b), and another with a reduction in spreading velocity at the base of the lithosphere due to lithospheric stretching to be applied beneath the Thetis-Nereus inter-trough (Figure 6c).

[37] We considered first a steady state mantle flow induced by motion of the overlying rigid plates in an incompressible, homogeneous, isoviscous mantle. The steady state three-dimensional passive mantle flow has been solved via the Fourier pseudo-spectral technique outlined in *Ligi et al.* [2008] both for thin plates and for plates that thicken away from the ridge.

[38] In order to estimate the mantle long-term thermal gravity signal in a flow model that is passive within an upper layer and active below, we modified the passive flow half-space solutions of *Ligi et al.* [2008]. We assumed as boundary condition for the lower limit of the upper layer, mantle velocities from an upwelling divergent flow. The upwelling divergent flow model [*Kuznir and Karner*, 2007] is based on the two-dimensional corner-flow solution [*Reid and Jackson*, 1981] and simulates both passive and active mantle flows depending on the boundary conditions. Boundary conditions include the velocity field at the surface, defined by the half spreading rate $V_x^0(x,z = 0)$, and the axial upwelling rate $V_z^0(x = 0,z)$, defined by the V_z^0/V_x^0 ratio. For V_z^0/V_x^0 ratios less than 1.5, the model produces passive mantle flow solutions ($V_z^0/V_x^0 = 2/\pi$ is the thin plate solution); for higher ratios the model generates active flows [*Fletcher et al.*, 2009].

[39] Passive flow temperature solutions were obtained assuming a temperature of 0°C at the surface and a constant mantle temperature, ranging from 1330°C to 1430°C, at the bottom of the model (depth 150 km). Potential temperature is the temperature that a fluid mass would have if it were compressed or expanded to some constant reference pressure. Hereafter, we refer to mantle potential temperature at the reference pressure of 150 km depth. In the dynamic flow models, the temperature field has been modeled assuming different values for the V_z^0/V_x^0 ratio (ranging from $2/\pi$ to 4.5) and a reference mantle potential temperature of 1350°C (see next Chapter). Passive flow models (for a given mantle potential temperature) produce a thermal mantle contribution to the gravity field

smaller than mixed active-passive flow models at high V_z^0/V_x^0 ratios. Figures 6b and 6c show two examples (possible end-members) of the predicted thermal mantle gravity field for a plate thickening passive flow and a mixed plate-thickening/upwelling-divergent flow, respectively. Plate separation velocities at the base of the lithosphere are as indicated in the figures (plate boundary geometry model I and II) and the temperature at the base of the computational box is 1350°C for both models. In the mixed active-passive model, we assumed that passive flow velocities at a depth z = 60 km (base of the dry melting region), are those of an upwelling divergent flow model computed at the same depth with V_z^0/V_x^0 = 4, beneath a mean spreading axis (Figure 11b). Given the small offset segmentation of Thetis and Nereus spreading segments, the three-dimensional mantle flow perturbation due to transform offsets is soon smoothed out with depth, allowing to combine the two-dimensional solutions of the upwelling divergent flow with those (three-dimensional) of passive flow. The inferred crustal thickness variations are shown in Figures 11c and 11d. Note that the mantle thermal contribution is a long wavelength correction and has little effect on the short wavelength relative variations of the MBA that affect mostly the inferred crustal thickness variations. Our gravity inversion close to rift axis is robust and is not affected much by the long-term mantle thermal correction, regardless of the mantle flow models adopted to define the underlain thermal structure.

4.2. Melting Modeling

[40] Models of mantle flow were tested against the melting parameters inferred from basalt geochemistry. We carried out numerical experiments to estimate mean degree of melting, mean pressure of melting, and mean composition of the aggregate melt beneath a spreading axis. Following *Ligi et al.* [2005], we modeled melt generation including the effect of water on the peridotite solidus, using a modified parameterization of experimental data developed by *Katz et al.* [2003], adding a pressure-dependent H_2O bulk distribution coefficient [*Hirth and Kohlstedt*, 1996]. We varied the H_2O content in the upper mantle from 0.005 to 0.025 wt%; mantle mineral assemblages for garnet, spinel, and plagioclase peridotite facies are taken from *McKenzie and O'Nions* [1991]. REE distribution coefficients and source contents are from *Hellebrand et al.* [2002]. We assumed that mineral proportions in the transition zone between 85 and 60 km, vary linearly from pure garnet peridotite to pure spinel peridotite. Moreover, we assumed pure-fractional melting and complete melt extraction, but we neglected latent heat of fusion by freezing of melt and hydrothermal cooling. Given that H_2O is about as incompatible as Ce [*Asimow and Langmuir*, 2003], its concentration in the aggregate liquid is inversely proportional to the mean extent of melting. The amount of water contained in the aggregated melt has been estimated by varying mean degree of melting and mantle source water content (Table 3 and Figure 12a). Thus, the water content of the basaltic glasses constrains the amount of water contained in the mantle source of Thetis and Nereus basalts, ranging from 0,01 to 0,022 wt% (Figure 12a). We assumed a water content of 0.02 wt%, because it is the best fit to our data.

[41] Assuming the melting model outlined above and plate-thickening passive mantle flow, we have calculated that the crustal thickness measured in "normal" mid-ocean ridges at different spreading rates can be explained best by a mantle temperature of 1350°C at the base of model. Variations in the extent of melting have been obtained by varying mantle temperatures and mantle upwelling velocities for passive and dynamic mantle flows, respectively (Table 3). We adopted the reference potential temperature of 1350°C at a depth of 150 km in order to estimate melting parameters at different mantle upwelling velocities. The results show that, although the predicted Na_2O concentrations of the aggregated liquid are similar for a given degree of melting in both mantle flow regimes, the mean pressure of melting produces contrasting values and patterns in the two cases (Figure 13). The mean degree of melting for passive flow at fixed half spreading rate and mantle source composition increases with increasing temperature, deepening the peridotite solidus and the initiation of melting, thus increasing the mean melting pressure. Mantle modal and mineral composition (fertile against refractory mantle rocks) affects the mean degree and the mean pressure of melting, as does temperature. In contrast, for active flow at fixed potential temperature and composition of the mantle source, the extent of melting increases with increasing mantle upwelling rates. High upwelling velocities limit top-down lithospheric cooling and allow melting to proceed to shallow levels, thus decreasing the average pressure of melting. We will test next the predictions derived by these models with geochemical and geophysical data obtained from the Thetis and Nereus "oceanic" segments.
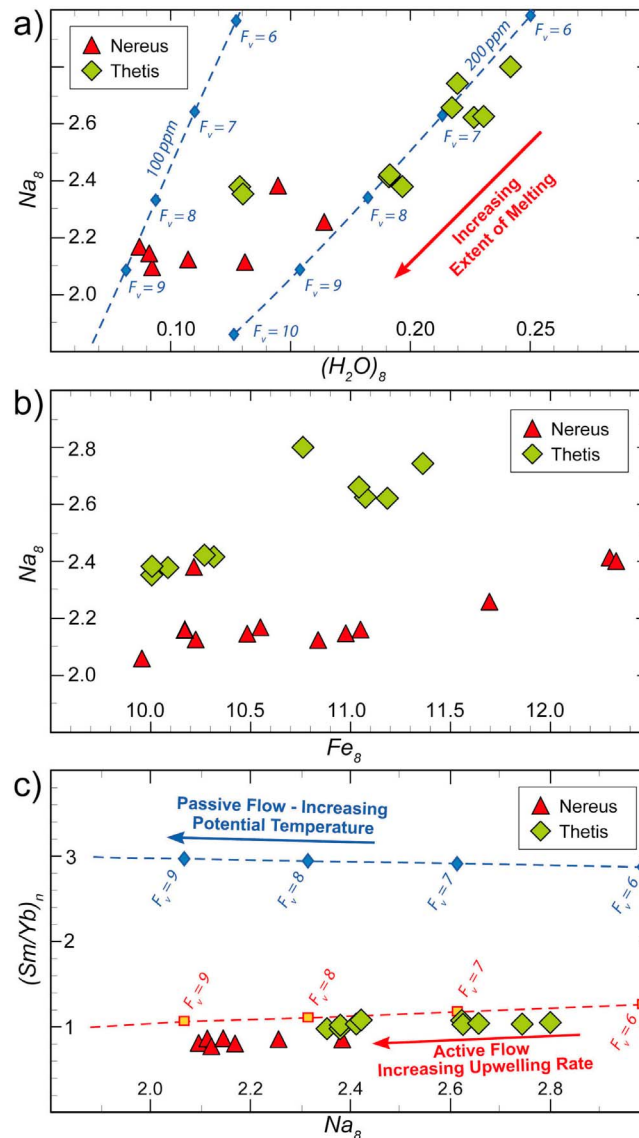
Figure 12. (a) Distribution of Na_8 and $(H_2O)_8$ in MORB glasses along the axis of Thetis and Nereus. Compositions at a common 8% MgO were calculated using for Na_2O the equation of *Plank and Langmuir* [1992], and for H_2O that of *Taylor and Martinez* [2003]. Blue diamonds represent the modeled water content of the aggregated melt for a given mean degree of melting (F_v) with mantle source of N-MORB assumed to contain 0.01 and 0.02 wt% H_2O. (b) Along axis distribution of Na_8 and Fe_8. FeO compositions at a common 8% MgO were calculated using the equation of *Klein and Langmuir* [1987]. Nereus basalts are originated from higher degrees of melting and from a wider range of melting pressures than Thetis basalts, suggesting sources with different fertility and/or mantle temperatures. (c) Observed and predicted chondrite normalized $(Sm/Yb)_n$ ratios vs Na_8. Blue diamonds and orange squares indicate predicted values at a given mean degree of melting from plate-thickening passive flow and dynamic mantle flow, respectively.

4.3. Initial Oceanic Crust Accretion

[42] The intensity of magnetization of the initial oceanic crust accreting today (i.e., <0.7 Ma) in the Thetis northern sub-basin and in the southern tip of Nereus, is almost twice that of the near-zero-age axial zones of the more evolved Thetis central and southern sub-basins, where the initial emplacement of oceanic crust occurred 1.6 and 2.2 Ma, respectively (Figure 8). This "initial" higher magnetization appears not to be due to crustal composition, because it is not associated with Fe-enriched basalts (Figure 10d); it is probably due to a thicker basaltic crust, as suggested independently also by the areal distribution of crustal thickness inferred from gravity (Figures 10a and 11).
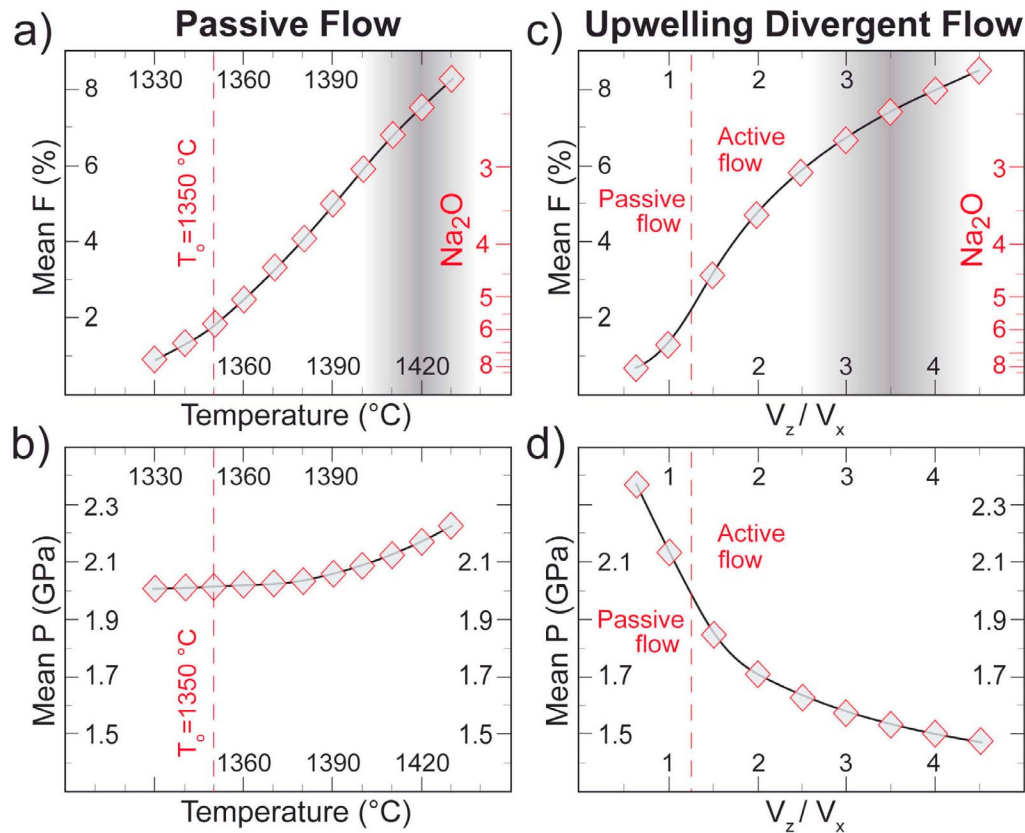
Figure 13. Predicted mean degree of melting, Na_2O content in the aggregated melt, and mean pressure of melting for different mantle flow regimes, assuming pure fractional wet melting and complete melt extraction. The gray shaded band marks the region where the generated melt shows predicted Na_2O contents, similar to those of Nereus and Thetis basaltic glasses. (a and b) Plate thickening passive mantle flow assuming a half spreading rate of 6.1 mm/a [*Chu and Gordon*, 1998]. Mantle temperatures were estimated by solving the steady state advection-diffusion equation, assuming 0°C at the seafloor and temperatures ranging from 1330°C to 1430°C at 150 km of depth. The reference mantle potential temperature of 1350°C is indicated by a red dashed line. (c and d) Upwelling divergent flow assuming a half plate separation velocity (V_x) of 6.1 mm/a. Melt generation has been modeled for mantle upwelling (V_z) and plate separation (V_x) velocity ratio ranging from $2/\pi$ to 4.5, assuming a mantle temperature of 1350°C at the depth of 150 km.

[43] Based on Na_8 data, "initial" oceanic basalts from areas of thicker crust (i.e., Thetis northern sub-basin and southern tip of Nereus) were generated by a degree of mantle melting higher than that of the basalts produced today in the more evolved portions of Thetis and Nereus (Figure 10c). Degree of melting versus age of the initial breakthrough of oceanic crust (i.e., age of the oldest Vine-Matthews magnetic anomalies for each spreading cell) shows that "initial" basalts were generated by a degree of melting higher than that of subsequent melts (Figure 10). The initial prevalence of smooth-textured sheet lava flows may also indicate initial eruption rates of hotter, fluid lavas faster than the subsequent hummocky-textured pillow flows erupting today on the axial volcanic ridge [*Bonatti and Harrison*, 1988; *Perfit and Chadwick*, 1998; *Cann and Smith*, 2005]. In addition, spreading both at

Thetis and Nereus was faster immediately after the initial breakthrough of oceanic crust (when mantle degree of melting and crustal thickness were also highest), and slowed down afterwards (Figure 8). Thus, an initial intense burst of oceanic crust generation and fast spreading takes place as soon as the lid of thinned continental lithosphere breaks and melt can be extracted efficiently at rift axes (Figure 14a).

4.3.1. What Causes the Initial Burst?

[44] We will attempt to constrain the subrift mantle processes that trigger the initial emplacement of oceanic crust. Either higher temperature/fertility of the passively ascending subrift asthenosphere, or its high, active ascending speed triggered by secondary convection could be responsible for the initial
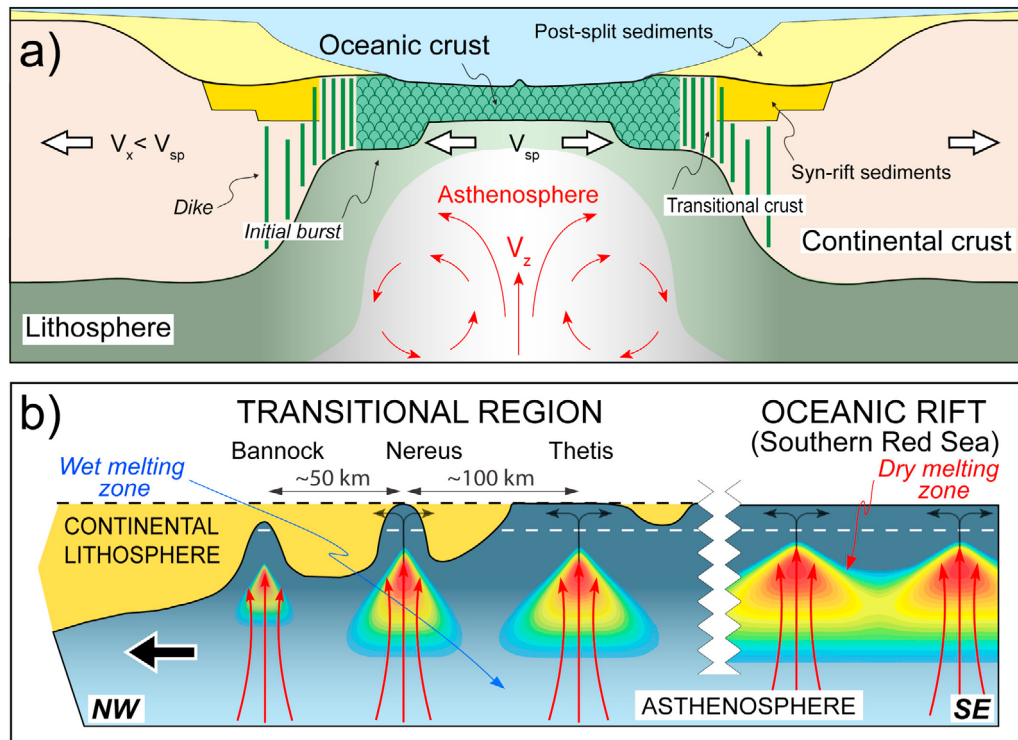
Figure 14. Continental to oceanic rift transition in the central Red Sea. During continental rifting, starting in Late Oligocene (~30 Ma) and proceeding for 20–15 Ma, a thermal/compositional anomaly probably related to the Afar plume, developed beneath the lithosphere. Increased temperatures deepen the solidus and favor short-lived small-scale convection by locally decreasing viscosity and increasing buoyancy of the upwelling asthenosphere. (a) At the onset of seafloor spreading, the strong horizontal thermal gradient enhances edge driven mantle convection, causing an initial burst of oceanic crust injection, with high degree of melting, thick crust and fast spreading (northern Thetis stage). The pulse of high oceanic crust generation decays rapidly as the oceanic rift widens and the horizontal thermal gradient decreases, evolving into a more "passive" steady regime dictated by spreading rate (southern Thetis stage). V_{sp} is the oceanic crustal accretion rate, and V_x and V_z are plate separation and mantle upwelling velocities, respectively. (b) The solid mantle upwells in a series of closely spaced cells serving as nucleii for axial propagation of oceanic accretion, that evolves then in linear segments of spreading. White horizontal dashed line marks the lower boundary of the oceanic lithosphere.

pulse. As discussed in section 4.2, if the initial higher degree of mantle melting were due solely to a hotter upwelling mantle, peridotite solidus and initiation of melting would occur deeper in the mantle, thus increasing the average pressure of melting (Figure 13). We assume basalt Na_8 to be related the mean degree of melting of the mantle source, and Fe_8 to the mean pressure of melting [*Klein and Langmuir*, 1987]. Na_8 correlates positively with Fe_8 in basaltic glasses from Thetis and Nereus (Figure 12b), indicating that an increase in the degree of melting corresponds to a decrease in the mean pressure of melting. This suggests that faster mantle upwelling rather than high mantle temperature/fertility is responsible for the initial melting pulse. Two different positive trends can be distinguished looking separately at the samples from Thetis and from Nereus. The two slopes imply

that Nereus basalts originated from a slightly higher mantle degree of melting and a wider range of melting pressures than Thetis basalts. This suggests that each oceanic cell may tap mantle with slightly different fertility and/or temperature, but in each case mantle rises fast in the initial phase of opening.

4.3.2. Melting in the Garnet Stability Field

[45] Our numerical model for high degrees of melting predicts that passive flow generates melt deeper than dynamic flow (Figure 13). The deeper the level where the ascending mantle stops melting, the higher the proportion of melt generated in the presence of garnet [*Ellam*, 1992]. We would thus expect for passive flow a significant "garnet signature" in our basalts, since they are less diluted by melts produced in the "dry melting interval"

within the spinel stability field above ~60 km depth. REE partition coefficients during melting are different across the 85 to 60 km boundary between garnet stability below, and spinel stability above. Melting in the garnet stability field produces liquids depleted of HREE relative to LREE, with $(Sm/Yb)_n$ ratios well over one [*Gast*, 1968; *Anders and Grevesse*, 1989; *Shen and Forsyth*, 1995; *Hellebrand et al.*, 2001] and increasing with the proportion of melt generated in the garnet stability field. Figure 12c shows observed and predicted chondrite normalized $(Sm/Yb)_n$ ratios against Na_8 of Thetis and Nereus basaltic glasses. $(Sm/Yb)_n$ stays close to one and decreases with increasing degrees of melting, as predicted by the dynamic mantle flow model.

4.3.3. Fast Initial Mantle Upwelling

[46] All the above suggests that high extents of initial melting below Thetis and Nereus are due to enhanced mantle upwelling rates rather than to mantle source thermal or compositional variations. This "active" upwelling can be due either to cold-edge driven convection, or to depletion/melt-retention buoyancy driven convection. Our results suggest a transient high magmatic productivity as the lid of continental lithosphere breaks, followed by steady crustal accretion. Our preferred explanation of these results is that post-breakup initial mantle upwelling below Thetis and Nereus is enhanced because a sharp horizontal thermal gradient between the thick/cold continental lithosphere and the hot melt-rich low-viscosity ascending asthenosphere can trigger secondary small-scale edge-driven mantle convection [*Ligi et al.*, 2011]. Numerical models of small-scale edge-driven convection during rifting and breakup including narrow necking regions [*Keen and Boutilier*, 1995], and of convection near steep lithospheric boundaries [*Buck*, 1986; *King and Anderson*, 1998] show high upwelling rates within a certain range of viscosities. These models do not include melting and it is unlikely that the high upwelling rates reach shallow enough depths to produce significant amount of melt. Simulations of convective flow near mid ocean ridges have shown that buoyant flow is created mostly by the buoyancy of retained melt and residual mantle, and by the viscosity variations due to mantle source water content and melt generation [*Sotin and Parmentier*, 1989; *Scott and Stevenson*, 1989; *Buck and Su*, 1989; *Choblet and Parmentier*, 2001]. Models of edge-driven convection that include melting and a viscosity increase due to dehydration caused by melting, do simulate the transient high melt production at

break-up, followed by stabilization of the flow and reduction of fluctuations in upwelling velocity after the initial pulse of magmatism [*Boutilier and Keen*, 1999; *Nielsen and Hopper*, 2004]. The return flow required to develop this small-scale convection is due to thermal and compositional buoyancy beneath the upwelling center and cooling of the residual mantle away from the ridge (Figure 14a). This upwelling component weakens as the oceanic rift widens, because the horizontal thermal gradient decreases. In addition, the subrift buoyant residual mantle resists small-scale convection. Thus, mantle upwelling and crustal accretion settle rapidly into a more steady regime. Numerical models have shown that the crust produced by this mechanism can be up to 35% thicker than steady state crustal production [*Nielsen and Hopper*, 2004], consistent with our crustal thickness data.

[47] We found in southern Thetis and central Nereus higher spreading rates during the initial phases of oceanic crustal emplacement, whereas spreading rates for the Bruhnes epoch (<0.78 Ma) slow down to 8 and 10 mm/a, close to the Nubia and Africa separation velocity of 9.4 mm/a inferred from GPS measurements [*McClusky et al.*, 2003]. However, the average full spreading rates we measured of 16 and 20 mm/a for southern Thetis and central Nereus, respectively, are higher than the average plate separation velocity (last 3 Ma) of 12.2 mm/a estimated from Euler vectors of *Chu and Gordon* [1998]. A crustal spreading velocity higher than plate separation velocity implies compressive deformation at the margins. Models of continental breakup involving divergent asthenospheric flow [*Kuznir and Karner*, 2007] are capable of inducing compressive deformation at the margins, where the rate of divergent flow exceeds the rate of plate separation. Compression, to be expected primarily at or close to the time of breakup, could explain early Cenozoic deformation recorded offshore mid-Norway and in the Faroes–Rockall area [*Lundin and Doré*, 2002; *Johnson et al.*, 2005]. Post-breakup compressive deformation in the Red Sea syn-rift sediments would be hard to detect because structures within the sedimentary cover are over-printed by the intense salt tectonics affecting the Red Sea margins.

[48] The transition zone in the central Red Sea from full-thickness continental lithosphere to initial oceanic lithosphere is rather narrow (~50 km). Other margins, such as the >200 km wide Iberian margin, show wider continental/oceanic zone of transition [*Hopper and Buck*, 1998], with scarce or absent

initial oceanic basalt volcanism, slow initial spreading and mostly "passive" mantle upwelling [*Srivastava et al.*, 2000]. Secondary mantle convection, predicted below narrow rifts [*Buck*, 1986], should weaken as the oceanic rift widens, in line with the observation that the Red Sea initial melting/spreading pulse declines rapidly at each cell, and settle into a more "passive" steady regime [*Ligi et al.*, 2011]. Other areas of transition from continental to oceanic rift showing initial spreading faster than subsequent steady spreading include the eastern Gulf of Aden rift at magnetic anomaly c5Dn (~17 Ma) [*D'Acremont et al.*, 2006], as well as narrow Red Sea-type segments of continent-ocean transition during the Mesozoic separation of North America and Euro/Africa [*Armitage et al.*, 2009; *Withjack et al.*, 1998], in contrast with wide, Iberian-type rift segments. The "initial burst" effect may be superimposed in the Red Sea on mantle upwelling and melting affected by (a) the opening rate of the Red Sea rift that, given the location of the pertinent pole of rotation, decreases from south to north [*Chu and Gordon*, 1998]; and (b) the influence of the Afar plume, also decreasing from south to north [*Altherr et al.*, 1990].

4.4. Axial "Oceanic" Cells

[49] Our results confirm that the breakthrough of oceanic crust and the inception of seafloor spreading have not been synchronous along the Red Sea, but occurred initially in isolated cells (Figure 14b), that subsequently acted as nuclei for axial propagation resulting in a continuous accretionary boundary, as observed today in the southern Red Sea [*Bonatti*, 1985]. Our observations imply that first-order initial accretion cells (i.e., Tethis, Nereus etc) can develop secondary cells (i.e., central and northern Thetis subbasins). The discontinuous distribution of the oldest magnetic anomalies in the western (c5n, ~10 Ma) and eastern (c5Dn, ~17 Ma) Gulf of Aden [*D'Acremont et al.*, 2006; *Cochran*, 1981] implies initial discrete "oceanic" cells also in the Gulf of Aden rift.

[50] The distribution of initial "oceanic" cells in the Red Sea/Gulf of Aden rifts can be explained by buoyancy-driven convection of hot, melt rich, low viscosity asthenosphere beneath extending continental lithosphere [*Bonatti*, 1985; *Choblet and Parmentier*, 2001]. According to numerical models, centers of upwelling develop along axis by buoyancy of retained melt and reduced density of depleted mantle, forming regularly spaced convective rolls within the low-viscosity layer, where wet melting

occurs between 120 and 65 km depth. Wavelength of the mantle upwelling cells depends on the thickness of the low viscosity layer [*Whitehead et al.*, 1984; *Choblet and Parmentier*, 2001]. In the Red Sea, cells have wavelengths ranging from 50 to 100 km (Figure 14b). Their activation proceeded from south to north, from ~5–6 Ma at latitude ~16°–19°30′N, to <2 Ma in the Nereus cell at ~23°N. Another classical area of continental to oceanic rifting, i.e., the Gulf of California, differs from the Red Sea in that the opening is oblique, with transform boundaries separating short spreading centers. Equidistant cells of mantle dynamic upwelling along the axis of the Gulf of California, suggested by Rayleigh wave tomography [*Wang et al.*, 2009], are somewhat similar to the Red Sea upwelling cells, although with a different spacing.

[51] The distribution of asthenospheric upwellings and of initial oceanic segments can be affected by structures preexisting continental breakup [*Cochran*, 2005; *Crane and Bonatti*, 1987], such as the "accommodation zones" that cause segmentation of the East African Rift [*Ghebreab*, 1998; *Bosworth*, 1989; *Makris and Rhim*, 1991]. Analogue modeling, simulating extension in the presence of a subcrustal zone of weakness, produces regularly spaced "asthenospheric" upwellings that subsequently propagate in an extension-orthogonal direction [*Corti et al.*, 2003], duplicating in the laboratory the opening of the Red Sea rift. The Red Sea N-propagating oceanic rift may be impacting today against the Zabargad Fracture Zone (Figure 1), a major morphotectonic feature that intersects the Red Sea in a NNE direction offsetting the Red Sea axis by about 100 km, and representing probably the precursor to a large-offset oceanic transform [*Bonatti et al.*, 1986]. The island of Zabargad, an uplifted block of sub-Red Sea lithosphere, lies along the southern (African) end of this feature [*Bonatti et al.*, 1981, 1984], whereas Mabahiss Deep, located at its northern (Arabian) end, is interpreted as a pull-apart basin floored by basalts [*Guennoc et al.*, 1988, 1990; *Coutelle et al.*, 1991], probably the northernmost occurrence of oceanic crust in the Red Sea. Zabargad island exposes a Panafrican metagranitic unit crisscrossed by Cenozoic basaltic dikes [*Bonatti and Seyler*, 1987], probably an example of the sub Red Sea crust outside the "oceanic" axial segments.

5. Conclusions

[52] The initial emplacement of oceanic crust in the Red Sea occurs in regularly spaced discrete "cells"

[53] serving as nucleii for axial propagation of oceanic accretion, that evolve then in linear segments of spreading. This segmentation may derive from regularly spaced centers of upwelling due to buoyancy-driven convection of hot, low viscosity asthenosphere beneath the extending continental lithosphere, influenced also by pre-existing structural features, such as continental rift initial "accommodation zones."

[53] Accretion of oceanic crust in the two northernmost cells (Thetis and Nereus) started roughly 2.2 and 2 Ma, respectively, and continues today. The Thetis segment is made by coalescence of three sub-cells that become shallower and narrower from south to north. The "inter-trough zones" that separate the Thetis axial "oceanic" cell from the Nereus cell to the north, and the Hadarba cell to the south, are devoid of magnetic anomalies and contain thick sediment sequences and relicts of continental crust. The Red Sea central depressed region broadens significantly in the inter-trough zones relative to the "oceanic" segments, indicating that deformation becomes focused in a narrow axial zone as soon as oceanic accretion starts.

[54] Geochemistry of Thetis and Nereus basaltic glasses suggests a rather sharp rift-to-drift transition marked by magmatic activity with typical MORB signature and a relatively high degree of mantle melting, with no contamination by continental lithosphere, suggesting that lower crust and mantle lithosphere have been replaced by upwelling asthenosphere already before the Nubia and Arabian plates separated. This is consistent with a rift model where depth-dependent extension, due to decoupling between the upper and lower lithosphere, results in mantle-lithosphere necking breakup before crustal-necking breakup. According to Na_8-Fe_8 data Nereus basalts originated from a slightly higher degree of mantle melting and a wider range of melting pressures than Thetis basalts, suggesting that each oceanic cell may tap mantle with slightly different fertility and/or temperature.

[55] Magnetic anomalies show a south to north time progression of the initial emplacement of oceanic crust within the Red Sea system. Mantle upwelling and melting may be affected by the south-north decreasing opening rate of the Red Sea and by the influence of the Afar plume, also decreasing from south to north. The northward propagation of oceanic accretion is today impacting against the Zabargad Fracture Zone, a morphotectonic feature that intersects the Red Sea in a NNE-SSW direction offsetting its axis.

[56] Eruption rate, spreading rate, magnetic intensity, crustal thickness and degree of melting of the sub-axial upwelling mantle are highest in the very initial phases of oceanic crust accretion both at Thetis and Nereus, following immediately continental breakup. This suggests a burst of "active" mantle upwelling with high degree of melting and fast spreading at the onset of oceanic crust injection both at Thetis and Nereus. This initial pulse was probably caused by secondary sub-rift mantle convection triggered by a sharp horizontal thermal gradient; it is followed by steady "passive" drifting. This mode of initial oceanic crust accretion may have been common in Mesozoic, Atlantic-type rifts, together with wider, amagmatic, Iberian-type continent-ocean zones of transition.

Acknowledgments

References

Altherr, R., F. Henjes-Kunst, H. Puchelt, and A. Baumann (1990), Volcanic activity in the Red Sea axial trough: Evidence for a large mantle diapir, *Tectonophysics*, *150*, 121–133.

Anders, E., and N. Grevesse (1989), Abundances of the elements: Meteoritic and solar, *Geochim. Cosmochim. Acta*, *53*, 197–214.

Antonini, P., R. Petrini, and G. Contin (1998), A segment of sea-floor spreading in the central Red Sea: Basalts from the Nereus Deep (23°00′–23°20′N), *J. Afr. Earth Sci.*, *27*, 107–114.

Armitage, J. J., T. J. Henstock, T. A. Minshull, and J. R. Hopper (2009), Lithospheric controls on melt production during continental breakup at slow rates of extension: Application to the North Atlantic, *Geochem. Geophys. Geosyst.*, *10*, Q06018, doi:10.1029/2009GC002404.

Armitage, J. J., J. S. Collier, and T. A. Minshull (2010), The importance of rift history for volcanic margin formation, *Nature*, *465*, 913–917.

Asimow, P. D., and C. H. Langmuir (2003), The importance of water to oceanic mantle melting regimes, *Nature*, *421*, 815–820.

Baker, J., L. Snee, and M. Menzies (1996), A brief Oligocene period of flood volcanism in Yemen: Implications for the duration and rate of continental flood volcanism at the

Afro-Arabian triple junction, *Earth Planet. Sci. Lett.*, *138*, 39–55.

Barberi, F., and J. Varet (1977), Volcanism of Afar—Small scale plate tectonics implications, *Geol. Soc. Am. Bull.*, *88*, 1251–1266.

Bartov, Y., G. Steinitz, M. Eyal, and U. Eyal (1980), Sinistral movement along the Gulf of Aqaba—Its age and relation to the opening of the Red Sea, *Nature*, *285*, 220–221.

Barzaghi, R., A. Fermi, S. Tarantola, and F. Sansò (1993), Spectral techniques in inverse Stokes and over-determined problems, *Surv. Geophys.*, *14*, 461–475.

Bialas, R. W., W. R. Buck, and R. Qin (2010), How much magma is required to rift a continent?, *Earth Planet. Sci. Lett.*, *292*, 68–78.

Blackman, D. K., and D. W. Forsyth (1992), The effects of plate thickening on three-dimensional, passive flow of the mantle beneath mid-ocean ridges, in *Mantle Flow and Melt Generation at Mid-Ocean Ridges*, *Geophys. Monogr. Ser.*, vol. 71, edited by J. Phipps Morgan, D. K. Blackman, and J. K. Sinton, pp. 311–326, AGU, Washington, D. C.

Boillot, G., S. Grimaud, A. Mauffret, D. Mougenot, J. Kornprobst, J. Mergoil-Daniel, and G. Torrent (1980), Ocean–continent boundary off the Iberian Margin: A serpentinite diapir west of the Galicia Bank, *Earth Planet. Sci. Lett.*, *48*, 23–34.

Boillot, G., et al. (1987), Tectonic denudation of the upper mantle along passive margins: A model based on drilling results (ODP leg 103, western Galicia margin, Spain), *Tectonophysics*, *132*, 335–342.

Bonatti, E. (1985), Punctiform initiation of seafloor spreading in the Red Sea during transition from continental to an oceanic rift, *Nature*, *316*, 33–37.

Bonatti, E., and C. G. A. Harrison (1988), Eruption styles of oceanic basalt in oceanic spreading ridges and seamounts: Effect of magma temperature and viscosity, *J. Geophys. Res.*, *93*, 2967–2980.

Bonatti, E., and M. Seyler (1987), Crustal underplating and evolution in the Red Sea rift, *J. Geophys. Res.*, *92*, 12,803–12,821.

Bonatti, E., P. Hamlyn, and G. Ottonello (1981), Upper mantle beneath a young oceanic rift—Peridotites from the island of Zabargad (Red Sea), *Geology*, *9*, 474–479.

Bonatti, E., P. Colantoni, B. Della Vedova, and M. Taviani (1984), Geology of the Red Sea transitional region (22°–25°N), *Oceanol. Acta*, *7*, 385–398.

Bonatti, E., G. Ottonello, and P. R. Hamlyn (1986), Peridotites from the island of Zabargad (Red Sea), *J. Geophys. Res.*, *91*, 599–631.

Bonatti, E., M. Ligi, D. Brunelli, A. Cipriani, P. Fabretti, V. Ferrante, L. Gasperini, and L. Ottolini (2003), Mantle thermal pulses below the Mid-Atlantic Ridge and temporal variations in the formation of oceanic lithosphere, *Nature*, *423*, 499–505.

Bosworth, W. (1989), Basin and range style tectonics in East Africa, *J. Afr. Earth Sci.*, *8*(2–4), 191–201.

Bosworth, W., P. Huchon, and K. McClay (2005), The Red Sea and Gulf of Aden basins, *J. Afr. Earth Sci.*, *43*, 334–378.

Bottazzi, P., L. Ottolini, R. Vannucci, and A. Zanetti (1994), An accurate procedure for the quantification of rare earth elements in silicates, in *IX International Conference on Secondary Ion Mass Spectrometry, Yokohama (Japan), Nov. 7–12 (1993)*, edited by A. Benninghoven et al., pp. 927–930, John Wiley, Chichester, U. K.

Boutilier, R. R., and C. E. Keen (1999), Small scale convection and divergent plate boundaries, *J. Geophys. Res.*, *104*, 7389–7403.

Braun, M. G., G. Hirth, and E. M. Parmentier (2000), The effect of deep damp melting on mantle flow and melt generation beneath mid-ocean ridges, *Earth Planet. Sci. Lett.*, *176*, 339–356.

Buck, W. R. (1986), Small-scale convection induced by passive rifting: The cause for uplift of rift shoulders, *Earth Planet. Sci. Lett.*, *77*, 362–372.

Buck, W. R., and W. Su (1989), Focused mantle upwelling below mid-ocean ridges due to feedback between viscosity and melting, *Geophys. Res. Lett.*, *16*(7), 641–644.

Cande, S. C., and D. V. Kent (1995), Revised calibration of the geomagnetic polarity timescale for the Late Cretaceous and Cenozoic, *J. Geophys. Res.*, *100*, 6093–6095.

Cann, J. R., and D. K. Smith (2005), Evolution of volcanism and faulting in a segment of the Mid-Atlantic Ridge at 25°N, *Geochem. Geophys. Geosyst.*, *9*, Q09008, doi:10.1029/2005GC000954.

Cannat, M., D. Sauter, J. Escartín, L. Lavier, and S. Picazo (2009), Oceanic corrugated surfaces and the strength of the axial lithosphere at slow spreading ridges, *Earth Planet. Sci. Lett.*, *288*, 174–183, doi:10.1016/j.epsl.2009.09.020.

Caratori Tontini, F., L. Cocchi, and C. Carmisciano (2009), Rapid 3-D forward model of potential fields with application to Palinuro Seamount magnetic anomaly (southern Tyrrhenian Sea, Italy), *J. Geophys. Res.*, *114*, B02103, doi:10.1029/2008JB005907.

Chang, S. J., and S. Van der Lee (2011), Mantle plumes and associated flow beneath Arabia and East Africa, *Earth Planet. Sci. Lett.*, *302*, 448–454.

Chang, S. J., M. Merino, S. Van der Lee, S. Stein, and C. A. Stein (2011), Mantle flow beneath Arabia offset from the opening Red Sea, *Geophys. Res. Lett.*, *38*, L04301, doi:10.1029/2010GL045852.

Choblet, G., and E. M. Parmentier (2001), Mantle upwelling and melting beneath slow spreading centers: Effects of variable rheology and melt productivity, *Earth Planet. Sci. Lett.*, *184*, 589–604.

Chu, D., and R. G. Gordon (1998), Current plate motions across the Red Sea, *Geophys. J. Int.*, *135*, 313–328.

Cipriani, A., E. Bonatti, D. Brunelli, and M. Ligi (2009), 26 million years of mantle upwelling below a segment of the Mid Atlantic Ridge: The Vema Lithospheric Section revisited, *Earth Planet. Sci. Lett.*, *285*, 87–95, doi:10.1016/j.epsl.2009.05.046.

Cochran, J. R. (1981), The Gulf of Aden: Structure and evolution of a young ocean basin and continental margin, *J. Geophys. Res.*, *86*, 263–287.

Cochran, J. R. (2005), Northern Red Sea: Nucleation of an oceanic spreading center within a continental rift, *Geochem. Geophys. Geosyst.*, *6*, Q03006, doi:10.1029/2004GC000826.

Coleman, R. G. (1974), Geologic background of the Red Sea, *Initial Rep. Deep Sea Drill. Proj.*, *23*, 813–819.

Coleman, R. G., and A. V. McGuire (1988), Magma systems related to the Red Sea opening, *Tectonophysics*, *150*, 77–100.

Cordery, M. J., and J. P. Morgan (1992), Melting and mantle flow beneath a mid-ocean spreading center, *Earth Planet. Sci. Lett.*, *111*(2–4), 493–516.

Cordery, M. J., and J. P. Morgan (1993), Convection and melting at mid-ocean ridges, *J. Geophys. Res.*, *98*(B11), 19,477–19,504.

Corti, G., J. Van Wijk, M. Bonini, D. Sokoutis, S. Cloethingh, F. Innocenti, and P. Manetti (2003), Transition from continental break-up to punctiform seafloor spreading: How fast, symmetric and magmatic, *Geophys. Res. Lett.*, *30*(12), 1604, doi:10.1029/2003GL017374.

Corti, G., J. van Wijk, S. Cloetingh, and C. K. Morley (2007), Tectonic inheritance and continental rift architecture: Numerical and analogue models of the East African Rift system, *Tectonics*, *26*, TC6006, doi:10.1029/2006TC002086.

Coulie, E., X. Quidelleur, P. Y. Gillot, V. Courtillot, J. C. Lefevre, and S. Chiesa (2003), Comparative K-Ar and Ar/Ar dating of Ethiopian and Yemenite Oligocene volcanism: Implications for timing and duration of the Ethiopian traps, *Earth Planet. Sci. Lett.*, *206*, 477–492.

Courtillot, V. (1982), Propagating rifts and continental breakup, *Tectonics*, *1*, 239–250.

Coutelle, A., G. Pautot, and P. Guennoc (1991), The structural setting of the Red-Sea axial valley and deeps–Implications for crustal thinning processes, *Tectonophysics*, *198*, 395–409.

Crane, K., and E. Bonatti (1987), The role of fracture zones during early Red Sea rifting: Structural analysis using Space Shuttle radar and LANDSAT imagery, *J. Geol. Soc.*, *144*, 407–420.

D'Acremont, E., S. Leroy, M. Maia, P. Patriat, M. O. Berslier, N. Bellahsen, M. Fournier, and P. Gente (2006), Structure and evolution of the eastern Gulf of Aden: Insights from magnetic and gravity data, *Geophys. J. Int.*, *165*, 786–803.

DeMets, C., R. G. Gordon, D. F. Argus, and S. Stein (1994), Effect of recent revisions to the geomagnetic reversal time scale on estimates of current plate motions, *Geophys. Res. Lett.*, *21*, 2191–2194.

Dixon, T. H., R. J. Stern, and I. M. Hussein (1987), Control of Red Sea rift geometry by pre-Cambrian structures, *Tectonics*, *6*, 551–571.

Drake, C. L., and R. W. Girdler (1964), A geophysical study of the Red Sea, *Geophys. J. R. Astron. Soc.*, *8*, 473–495.

Ebinger, C. J., and N. H. Sleep (1998), Cenozoic magmatism throughout east Africa resulting from impact of a single plume, *Nature*, *395*, 788–791.

Ebinger, C., A. Ayele, D. Keir, J. Rowland, G. Yirgu, T. Wright, M. Belachew, and I. Hamling (2010), Length and timescales of rift faulting and magma intrusion: The Afar rifting cycle from 2005 to present, *Annu. Rev. Earth Planet. Sci.*, *38*, 439–466.

Eldholm, O., and K. Grue (1994), North Atlantic volcanic margins: Dimensions and production rates, *J. Geophys. Res.*, *99*, 2955–2968.

Ellam, R. M. (1992), Lithospheric thickness as a control on basalt geochemistry, *Geology*, *20*, 153–156.

Feraud, G., V. Zumbo, A. Sebai, and H. Bertrand (1991), $^{40}Ar/^{39}Ar$ age and duration of tholeiitic magmatism related to the early opening of the Red Sea rift, *Geophys. Res. Lett.*, *18*, 195–198.

Fletcher, R., N. Kusznir, and M. Cheadle (2009), Melt initiation and mantle exhumation at the Iberian rifted margin: Comparison of pure-shear and upwelling-divergent flow models of continental breakup, *C. R. Geosci.*, *341*, 394–405.

Forsyth, D. W. (1992), Geophysical constraints of mantle flow and melt generation beneath mid-ocean ridges, in *Mantle Flow and Melt Generation at Mid-Ocean Ridges*, *Geophys. Monogr. Ser.*, vol. 71, edited by J. Phipps Morgan, D. K. Blackman, and J. K. Sinton, pp. 1–65, AGU, Washington, D. C.

Freund, R., I. Zak, and Z. Garfunkel (1968), Age and rate of the sinistral movement along the Dead Sea Rift, *Nature*, *220*, 253–255.

Gast, P. (1968), Trace element fractionations and the origin of tholeitic and alkaline magma types, *Geochim. Cosmochim. Acta*, *32*, 1057–1086.

Ghebreab, W. (1998), Tectonics of the Red Sea region reassessed, *Earth Sci. Rev.*, *45*, 1–44.

Girdler, R. W., and P. Styles (1974), Two stage seafloor spreading, *Nature*, *247*, 7–11.

Guennoc, P., G. Pautot, and A. Coutelle (1988), Surficial structures of the northern Red Sea axial valley from 23°N to 28°N: Time and space evolution of neo-oceanic structures, *Tectonophysics*, *153*, 1–23.

Guennoc, P., G. Pautot, M. F. Leqentrec, and A. Coutelle (1990), Structure of an early oceanic rift in the northern Red Sea, *Oceanol. Acta*, *13*, 145–157.

Hansen, S. E., A. J. Rodgers, S. Y. Schwartz, and A. M. S. Al-Amri (2007), Imaging ruptured lithosphere beneath the Red Sea and Arabian Peninsula, *Earth Planet. Sci. Lett.*, *259*, 256–265.

Hellebrand, E., J. E. Snow, H. J. B. Dick, and A. W. Hofmann (2001), Coupled major and trace elements as indicators of the extent of melting in mid-ocean-ridge peridotites, *Nature*, *410*, 677–681.

Hellebrand, E., J. E. Snow, P. Hoppe, and A. W. Hofmann (2002), Garnet-field melting and late-stage refertilization in "residual" abyssal peridotites from the central Indian Ridge, *J. Petrol.*, *43*, 2305–2338.

Hirth, G., and D. L. Kohlstedt (1996), Water in the oceanic upper mantle: Implications for rheology, melt extraction and the evolution of the lithosphere, *Earth Planet. Sci. Lett.*, *144*, 93–108.

Hofmann, C., V. Courtillot, G. Feraud, P. Rochette, G. Yirgu, E. Ketefo, and R. Pik (1997), Timing of the Ethiopian flood basalt event and implications for plume birth and global change, *Nature*, *389*, 838–841.

Hopper, J. R., and W. R. Buck (1998), Styles of extensional decoupling, *Geology*, *26*, 699–702.

Huang, M. T., Z. Guan, G. J. Zhai, and Y. Z. Ouyang (1999), On the compensation of systematic errors in marine gravity measurements, *Mar. Geod.*, *22*, 183–194.

Huismans, R., and C. Beaumont (2011), Depth-dependent extension, two-stage breakup and cratonic underplating at rifted margins, *Nature*, *473*(7345), 74–78.

Hwang, C., and B. Parsons (1995), Gravity anomalies derived from Seasat, Geosat, ERS-1 and TOPEX/POSEIDON altimetry and ship gravity: A case study over the Reykjanes Ridge, *Geophys. J. Int.*, *122*, 551–568.

Izzeldin, A. Y. (1982), On the structure and evolution of the Red Sea, PhD thesis, 164 pp., Inst. de Phys. du Globe, Strasbourg, France.

Izzeldin, A. Y. (1987), Seismic, gravity and magnetic surveys in the central part of the Red Sea: Their interpretation and implications for the structure and evolution of the Red Sea, *Tectonophysics*, *143*, 269–306.

Izzeldin, A. Y. (1989), Transverse structures in the central part of the Red Sea and implications on early stages of oceanic accretion, *Geophys. J. Int.*, *96*, 117–129.

Jagoutz, O., O. Müntener, G. Manatschal, D. Rubatto, G. Peron-Pinvidic, B. D. Turrin, and I. M. Villa (2007), The rift-to-drift transition in the North Atlantic: A stuttering start of the MORB machine?, *Geology*, *35*, 1087–1090.

Johnson, H., J. D. Ritchie, K. Hitchen, D. B. McInroy, and G. S. Kimbell (2005), Aspects of the Cenozoic deformational history of the Northeast Faroe-Shetland Basin, Wyville-Thomson Ridge and Hutton Bank areas, in *Petroleum Geology: North- West Europe and Global Perspectives. Proceedings of the 6th Petroleum Geology Conference*, edited by A. G. Doré and B. A. Vining, pp. 993–1008, Geol. Soc., London.

Katz, R. F., M. Spiegelman, and C. H. Langmuir (2003), A new parameterization of hydrous mantle melting, *Geochem. Geophys. Geosyst.*, *4*(9), 1073, doi:10.1029/2002GC000433.

Keen, C. E., and R. R. Boutilier (1995), Lithosphere-asthenosphere interactions below rifts, in *Rifted Ocean-Continent Boundaries*, edited by E. Banda, M. Torne, and M. Talwani, pp. 17–30, Kluwer Acad., Norwell, Mass.

Keir, D., M. Belachew, C. J. Ebinger, J. Kendall, J. O. S. Hammond, G. W. Stuart, and A. Ayele (2011), Mapping the evolving strain field in the Afar Triple Junction using crustal anisotropy, *Nat. Commun.*, *2*, 285, doi:10.1038/ncomms1287.

Khalil, S. M., and K. R. McClay (2001), Tectonic evolution of the NW Red Sea-Gulf of Suez rift system, in *Non-Volcanic Rifting of Continental Margins*, edited by R. C. L. Wilson et al., *Geol. Soc. Spec. Publ.*, *187*, 453–473.

King, S. D., and D. L. Anderson (1998), Edge-driven convection, *Earth Planet. Sci. Lett.*, *160*, 289–296.

Klein, E. M., and C. H. Langmuir (1987), Global correlations of ocean ridge basalt chemistry with axial depth and crustal thickness, *J. Geophys. Res.*, *92*, 8089–8115.

Kroner, A., R. J. Stern, A. S. Dawoud, W. Compston, and T. Reischmann (1987), The Pan-African continental-margin in northeastern Africa—Evidence from a geochronological study of granulites at Sabaloka, Sudan, *Earth Planet. Sci. Lett.*, *85*, 91–104.

Kuznir, N. J., and G. D. Karner (2007), Continental lithospheric thinning and breakup in response to upwelling divergent mantle flow: Application to the Woodlark, Newfoundland and Iberia Margin, in *Imaging, Mapping and Modeling Continental Lithosphere Extension and Breakup*, edited by G. D. Karner, G. Manatschal, and L. M. Pinheiro, *Geol. Soc. Spec. Publ.*, *282*, 389–419.

Lavier, L. L., and G. Manatschal (2006), A mechanism to thin the continental lithosphere at magma-poor margins, *Nature*, *440*, 324–328.

Le Roux, V., J. L. Bodinier, A. Tommasi, O. Alard, J. M. Dautria, A. Vauchez, and A. J. V. Riches (2007), The Lherz spinel lherzolite: Refertilized rather than pristine mantle, *Earth Planet. Sci. Lett.*, *259*, 599–612.

Li, J., and M. G. Sideris (1997), Marine gravity and geoid determination by optimal combination of satellite altimetry and shipborne gravimetry data, *J. Geod.*, *71*, 209–216.

Ligi, M., and G. Bortoluzzi (1989), PLOTMAP: Geophysical and geological applications of good standard quality cartographic software, *Comput. Geosci.*, *15*, 519–585.

Ligi, M., E. Bonatti, A. Cipriani, and L. Ottolini (2005), Water-rich basalts at mid-ocean ridge cold spots, *Nature*, *434*, 66–69.

Ligi, M., M. Cuffaro, F. Chierici, and A. Calafato (2008), Three-dimensional passive mantle flow beneath mid-ocean ridges: An analytical approach, *Geophys. J. Int.*, *175*, 783–805.

Ligi, M., et al. (2011), Initial burst of oceanic crust accretion in the Red Sea due to edge-driven mantle convection, *Geology*, *39*, 1019–1022, doi:10.1130/G32243.1.

Lizarralde, D., et al. (2007), Variation in styles of rifting in the Gulf of California, *Nature*, *448*, 466–469.

Lundin, E. R., and A. G. Doré (2002), Mid-Cenozoic post-breakup deformation in the passive margins bordering the Norwegian-Greenland Sea, *Mar. Pet. Geol.*, *19*, 79–93.

Makris, M. J., and R. Rhim (1991), Shear controlled evolution of the Red Sea: Pull-apart model, *Tectonophysics*, *198*, 441–466.

Manatschal, G., N. Froitzheim, M. Rubenach, and B. D. Turrin (2001), The role of detachment faulting in the formation of an ocean-continent transition: Insights from the Iberia Abyssal Plain, in *Non-Volcanic Rifting of Continental Margins: A Comparison of Evidence from Land and Sea*, edited by R. C. L. Wilson et al., *Geol. Soc. Spec. Publ.*, *187*, 405–428.

McClusky, S., R. Reilinger, S. Mahmoud, D. Ben Sari, and A. Tealeb (2003), GPS constraints on Africa (Nubia) and Arabia plate motions, *Geophys. J. Int.*, *155*, 126–138.

McKenzie, D., and R. K. O'Nions (1991), Partial melt distributions from inversion of rare Earth Elements concentrations, *J. Petrol.*, *32*, 1021–1091.

Mitchell, N. C., M. Ligi, V. Ferrante, E. Bonatti, and E. Rutter (2010), Submarine salt flows in the central Red Sea, *Geol. Soc. Am. Bull.*, *122*, 701–713.

Mitchell, N. C., M. Schmidt, and M. Ligi (2011), Comment on "Formation of Thetis Deep metal-rich sediments in the absence of brines, Red Sea" by Pierret et al. (2010), *J. Geochem. Explor.*, *108*, 112–113.

Moretti, I., and B. Colletta (1987), Spatial and temporal evolution of the Suez Rift subsidence, *J. Geodyn.*, *7*, 151–168.

Morgan, J. P., and D. W. Forsyth (1988), Three-dimensional flow and temperature perturbations due to a transform offset: Effects on oceanic crustal and upper mantle structure, *J. Geophys. Res.*, *93*, 2955–2966.

Müntener, O., and G. Manatschal (2006), High degrees of melting recorded by spinel harzburgites of the Newfoundland margin: The role of inheritance and consequences for the evolution of the southern North Atlantic, *Earth Planet. Sci. Lett.*, *252*, 437–452.

Müntener, O., T. Pettke, L. Desmurs, M. Meier, and U. Schaltegger (2004), Refertilization of mantle peridotite in embryonic ocean basins: Trace element and Nd-isotope evidence and implications for crust-mantle relationships, *Earth Planet. Sci. Lett.*, *221*, 293–308.

Müntener, O., G. Manatschal, L. Desmurs, and T. Pettke (2010), Plagioclase peridotites in ocean-continent transitions: Refertilized mantle domains generated by melt stagnation in the shallow mantle lithosphere, *J. Petrol.*, *51*, 255–294, doi:10.1093/petrology/egp087.

Nielsen, T. K., and J. R. Hopper (2004), From rift to drift: Mantle melting during continental breakup, *Geochem. Geophys. Geosyst.*, *5*, Q07003, doi:10.1029/2003GC000662.

Omar, G. I., and M. S. Steckler (1995), Fission track evidence on the initial rifting of the Red Sea: Two pulses, no propagation, *Science*, *270*, 1341–1344.

Ottolini, L., P. Bottazzi, A. Zanetti, and R. Vannucci (1995), Determination of hydrogen in silicates by secondary ion mass spectrometry, *Analyst*, *120*, 1309–1313.

Pallister, J. S. (1987), Magmatic history of Red Sea rifting—Perspective from the central Saudi-Arabian coastal plain, *Geol. Soc. Am. Bull.*, *98*, 400–417.

Pallister, J. S., J. S. Stacey, L. B. Fischer, and W. R. Premo (1987), Arabian shield ophiolites and late Proterozoic microplate accretion, *Geology*, *15*, 320–323.

Pallister, J. S., et al. (2010), Broad accommodation of rift-related extension recorded by dike intrusion in Saudi Arabia, *Nat. Geosci.*, *3*, 705–712.

Parker, R. L. (1973), The rapid calculation of potential anomalies, *Geophys. J. R. Astron. Soc.*, *31*, 447–455.

Pautot, G. (1983), Red Sea deeps—A geomorphological study by Seabeam, *Oceanol. Acta*, *6*, 235–244.

Pedersen, T., and J. Skogseid (1989), Voring Plateau volcanic margin: Extension, melting and uplift, *Proc. Ocean Drill. Program Sci. Results*, *104*, 985–991.

Perfit, M. R., and W. W. Chadwick (1998), Magmatism at mid-ocean ridges: Constraints from volcanological and geochemical investigations, in *Faulting and Magmatism at Mid-Ocean Ridge*, *Geophys. Monogr. Ser.*, vol. 106, edited by W. R. Buck et al., pp. 59–116, AGU, Washington, D. C.

Pierret, M. C., N. Clauer, D. Bosch, and G. Blanc (2010), Formation of Thetis Deep metal-rich sediments in the absence of brines, Red Sea, *J. Geochem. Explor.*, *104*, 12–26.

Plank, T., and C. H. Langmuir (1992), Effects of the melting regime on the composition of oceanic crust, *J. Geophys. Res.*, *97*, 19,749–19,770.

Reid, I., and H. R. Jackson (1981), Oceanic spreading rate and crustal thickness, *Mar. Geophys. Res.*, *5*, 165–172.

Reston, T. J., and J. P. Morgan (2004), Continental geotherm and the evolution of rifted margins, *Geology*, *32*, 133–136.

Roeser, H. A. (1975), A detailed magnetic survey of the southern Red Sea, *Geol. Jahrb.*, *D13*, 131–153.

Ross, D. A., and J. Schlee (1973), Shallow structure and geologic development of the southern Red Sea, *Geol. Soc. Am. Bull.*, *84*, 3827–3848.

Rychert, C. A., J. O. S. Hammond, N. Harmon, J. M. Kendall, D. Keir, C. Ebinger, I. D. Bastow, A. Ayele, M. Belachew, and G. Stuart (2012), Volcanism in the Afar Rift sustained by decompression melting with minimal plume influence, *Nat. Geosci.*, *5*, 406–409, doi:10.1038/ngeo1455.

Said, R. (1969), General stratigraphy of the adjacent land areas of the Red Sea, in *Hot Brines and Recent Heavy Metal Deposits in the Red Sea*, edited by E. T. Degens and D. A. Ross, pp. 71–81, Springer, New York.

Sandwell, D. T., and W. H. F. Smith (1997), Marine gravity anomaly from Geosat and ERS-1 satellite altimetry, *J. Geophys. Res.*, *102*, 10,039–10,054.

Schmeling, H. (2010), Dynamic models of continental rifting with melt generation, *Tectonophysics*, *480*, 33–47.

Scholten, J. C., P. Stoffers, P. Walter, and W. Plüger (1991), Evidence for episodic hydrothermal activity in the Red Sea from the composition and formation of hydrothermal sediments, Thetis Deep, *Tectonophysics*, *190*, 109–117.

Scott, D. R., and D. J. Stevenson (1989), A self-consistent model of melting, magma migration and buoyancy-driven circulation beneath mid-ocean ridges, *J. Geophys. Res.*, *94*, 2973–2988.

Searle, R. C., and D. A. Ross (1975), A geophysical study of the Red Sea axial trough between 20.5° and 22°N, *Geophys. J. R. Astron. Soc.*, *43*, 555–572.

Sestini, J. (1965), Cenozoic stratigraphy and depositional history, Red Sea coast, Sudan, *Am. Assoc. Pet. Geol. Bull.*, *49*, 1453–1472.

Shen, Y., and D. W. Forsyth (1992), The effects of temperature and pressure dependent viscosity on three-dimensional passive flow of the mantle beneath a ridge-transform system, *J. Geophys. Res.*, *97*, 19,717–19,728.

Shen, Y., and D. W. Forsyth (1995), Geochemical constraints on initial and final depths of melting beneath mid-ocean ridges, *J. Geophys. Res.*, *100*, 2211–2237.

Sibuet, J. C., S. P. Srivastava, and G. Manatschal (2007), Exhumed mantle-forming transitional crust in the Newfoundland-Iberia rift and associated magnetic anomalies, *J. Geophys. Res.*, *112*, B06105, doi:10.1029/2005JB003856.

Sideris, M. G. (1996), On the use of heterogeneous noisy data in spectral gravity field modeling methods, *J. Geod.*, *70*, 470–479.

Sotin, C. J., and E. M. Parmentier (1989), Dynamical consequences of compositional and thermal density stratification beneath spreading centers, *Geophys. Res. Lett.*, *16*, 835–838.

Srivastava, S. P., J.-C. Sibuet, S. Cande, W. R. Roest, and I. D. Reid (2000), Magnetic evidence for slow seafloor spreading during the formation of the Newfoundland and Iberian margins, *Earth Planet. Sci. Lett.*, *182*, 61–76.

Steckler, M. S., F. Berthelot, N. Lyberis, and X. Le Pichon (1988), Subsidence in the Gulf of Suez: Implications for rifting and plate kinematics, *Tectonophysics*, *153*, 249–270.

Stern, R. J. (1994), Arc assembly and continental collision in the Neoproterozoic East African Orogen: Implications for the consolidation of Gondwanaland, *Annu. Rev. Earth Planet. Sci.*, *22*, 319–351.

Storey, B. C. (1995), The role of mantle plumes in continental break-up: Case histories from Gondwanaland, *Nature*, *377*, 301–308.

Sultan, M., R. Becker, R. E. Arvidson, P. Shore, R. J. Stern, Z. El Alfy, and R. I. Attia (1993), New constraints on Red Sea rifting from correlations of Arabian and Nubian Neoproterozoic outcrops, *Tectonics*, *12*, 1303–1319.

Taylor, B., and F. Martinez (2003), Back-arc basin basalt systematics, *Earth Planet. Sci. Lett.*, *210*, 481–497.

Tramontini, C., and D. Davis (1969), A seismic refraction survey in the Red Sea, *Geophys. J. R. Astron. Soc.*, *17*, 225–241.

Tziavos, I. N., M. G. Sideris, and R. Forsberg (1998), Combined satellite altimetry and shipborne gravimetry data processing, *Mar. Geod.*, *21*, 299–317.

Wang, Y., D. W. Forsyth, and B. Savage (2009), Convective upwelling in the mantle beneath the Gulf of California, *Nature*, *462*, 499–502.

White, R., and D. McKenzie (1989), Magmatism at rift zones: The generation of volcanic continental margins and flood basalts, *J. Geophys. Res.*, *94*, 7685–7729.

Whitehead, J. A., H. J. B. Dick, and H. Schouten (1984), A mechanism for magmatic accretion under spreading centres, *Nature*, *312*, 146–148.

Whiteman, A. J. (1968), Formation of the Red Sea depression, *Geol. Mag.*, *105*, 231–246.

Whitmarsh, R. B., et al. (1974), *Initial Reports of the Deep Sea Drilling Project*, vol. 23, 1180 pp., U.S. Gov. Print. Off., Washington, D. C.

Whitmarsh, R. B., G. Manatschal, and T. A. Minshull (2001), Evolution of magma-poor continental margins from rifting to seafloor spreading, *Nature*, *413*, 150–154.

Withjack, M. O., R. W. Schlische, and P. E. Olsen (1998), Diachronous rifting, drifting and inversion on the passive margin of central eastern North America: An analog for other passive margins, *AAPG Bull.*, *82*, 817–835.

Workman, R. K., and S. R. Hart (2005), Major and trace element composition of the depleted MORB mantle (DMM), *Earth Planet. Sci. Lett.*, *231*, 53–72.

Wright, T. J., C. J. Ebinger, J. Biggs, A. Ayele, G. Yirgo, D. Keir, and A. Stork (2006), Magma-maintained rift segmentation at continental rupture in the 2005 Afar diking episode, *Nature*, *442*, 291–294.

Zumbo, V., G. Feraud, H. Bertrand, and G. Chazot (1995), $^{40}Ar/^{39}Ar$ chronology of tertiary magmatic activity in southern Yemen during the early Red Sea–Aden rifting, *J. Volcanol. Geotherm. Res.*, *65*, 265–279.